



DOI: 10.29026/oea.2020.190038

# Printing photovoltaics by electrospray

Xinyan Zhao<sup>1,2</sup> and Weiwei Deng<sup>2\*</sup>

Solution processible photovoltaics (PV) are poised to play an important role in scalable manufacturing of low-cost solar cells. Electrospray is uniquely suited for fabricating PVs due to its several desirable characteristics of an ideal manufacturing process such as compatibility with roll-to-roll production processes, tunability and uniformity of droplet size, capability of operating at atmospheric pressure, and negligible material waste and nano structures. This review begins with an introduction of the fundamentals and unique properties of electrospray. We put emphasis on the evaporation time and residence time that jointly affect the deposition outcome. Then we review the efforts of electrospray printing polymer solar cells, perovskite solar cells, and dye sensitized solar cells. Collectively, these results demonstrate the advantages of electrospray for solution processed PV. Electrospray has also exhibited the capability of producing uniform films as well as nanostructured and even multiscale films. So far, the electrospray has been found to improve active layer morphology, and create devices with efficiencies comparable with that of spin-coating. Finally, we discuss challenges and research opportunities that enable electrospray to become a mainstream technique for industrial scale production.

**Keywords:** photovoltaics; electrospray; solution process; polymer solar cells; perovskite solar cells; dye sensitized solar cells

Zhao X Y, Deng W W. Printing photovoltaics by electrospray: a review. *Opto-Electron Adv* 3, 190038 (2020).

## Introduction

Photovoltaics (PV) are devices that directly convert the clean, renewable and abundant solar energy into electricity. In the past decade, solution processible photovoltaics (SPPV) has emerged as a strong contestant for low cost renewable energy technology as compared with copper indium gallium diselenide (CIGS) and GaAs thin film solar cells or polycrystalline silicon solar cells, which suffer from high cost due to the expensive and demanding clean room or vacuum environments. Three main types of solution processible solar cells are: polymer solar cells, perovskite solar cells, as well as dye sensitized solar cells (DSSC). Truly remarkable progresses have been achieved in each of the three types of cells, all of which have achieved power conversion efficiencies (PCEs) beyond 14%. For example, lead halide perovskites have attracted immense attention as PV materials owing to their many ideal optoelectronic properties such as high ambipolar

mobilities, efficient high light absorptions, and long charge-carrier diffusion lengths<sup>1,2</sup>. Moreover, lead halide perovskites are synthesized from inexpensive and earth-abundant materials by solution process at relatively low temperatures (<150 °C). Within ten years, the PCEs of perovskite solar cells have surged from 3.8% to a certified 23.7%<sup>3-5</sup>. Meanwhile, polymer solar cells have also experienced a breakthrough after the PCEs hovering near 10% from 2000~2010. The surge of new donor materials and non-fullerene acceptor (NFA) has pushed the PCEs beyond 16%<sup>6-8</sup>. In comparison, the interest in DSSC has faded considerably because the film is much thicker (10 micro meters vs ~100 nm for polymer or ~300 nm for perovskite) and other challenge such as the sealing of liquid phase of dye<sup>9</sup>. But it is the push to search for solid state dye that helped the discovery of perovskite solar cells. For the sake of completeness, we still include DSSCs in the scope of this review.

Compared to silicon based solar cells, the manufactur-

<sup>1</sup>Academy for Advanced Interdisciplinary Studies, Southern University of Science and Technology (SUSTech), Shenzhen 518055, China.

<sup>2</sup>Department of Mechanics and Aerospace Engineering, Southern University of Science and Technology (SUSTech), Shenzhen 518055, China.

\*Correspondence: W W Deng, E-mail: dengww@sustech.edu.cn

Received: 4 November 2019; Accepted: 8 January 2020; Published: 22 June 2020

ing process for solution-based photovoltaics is greatly simplified, since devices can be fabricated at low temperature and atmospheric pressure from minute amounts of low-cost, abundant raw materials. Moreover, solution processible solar cells are naturally capable of implementing roll-to-roll processes, using flexible substrates, and being more environmentally friendly. Therefore, solution processible solar cells promise vast reduction in manufacturing cost and are attractive from an industrial manufacturing process perspective.

To make SPPVs commercially viable, one of the remaining challenges is to find a low cost and scalable manufacturing process to replace spin coating, the laboratory scale standard technique. Two categories of scalable techniques for making thin films from liquid phase precursor have been investigated (i) continuous phase based methods including doctor blade or shearing plate coating<sup>10–13</sup> and slot-die coating<sup>14–16</sup>; and (ii) dispersed phase or droplet based method, such as inkjet printing<sup>17–19</sup> and spray coating<sup>20–23</sup>, which are able to deposit films conformally on non-flat substrate and are much more tolerant to the surface curvature, roughness and defects. Most spray techniques are pneumatically based and need intense gas flow to atomize, disperse, or/and blow-dry the liquid solution<sup>20,24</sup>. The rapid gas flow in the pneumatic spray may blow away droplets containing active layer precursors and cause significant waste of expensive materials. Electro spray, on the other hand, relies on electric fields solely to create quasi-monodisperse charged droplets<sup>25</sup>. The electrostatic attraction force between the substrate and droplet effectively minimize material waste<sup>26</sup>. In addition, electro spray also has the ability of working in non-vacuum environments, natural compatibility to roll-to-roll process, and added benefits from the electrical field including less material loss and nano structures. The electro spray is also found to improve the alignment and orientation of the polymer molecules, and overall device performance in certain cases. Therefore, electro spray has become a promising tool in SPPV fabrication (Table 1).

This review begins with a concise introduction of the electro spray fundamentals to enable the readers to understand the unique properties and advantages offered by the electro spray. This section also serves as a brief tutorial of electro spray in the context of material processing. Then the effort and progress of electro spray fabrication of polymer solar cells, perovskite solar cells and DSSCs are reviewed. These results illustrate the simplicity of fabricating those mainstream types of solution processible PVs.

Finally, we present summary and outlook of electro spray printing of photovoltaics.

## Fundamentals of electro spray as a material processing technique

### Overview of the cone-jet mode electro spray

Electro spray is a fluid dynamic phenomenon in which the electrohydrodynamic stress deforms the liquid meniscus into a conical shape with a fine jet emanating from the apex of the cone. This elegant process can generate monodispersed droplets of a few nm to 100  $\mu\text{m}$ . The superior capability of generating charged droplets in the nanometer range helped Prof. John B. Fenn to pioneer the electro spray ionization mass spectroscopy (ESI-MS)<sup>27</sup> that eventually brought him the Nobel Prize in Chemistry in 2002. A typical electro spray can be established by supplying a liquid with certain electric conductivity through a capillary charged to a voltage of a few kVs (Figs. 1 (a) and 1(b)). The liquid at the capillary end takes a conical shape, termed Taylor-cone<sup>28</sup>, which is due to the balance between surface tension and electric stress norm at the liquid-gas interface (Fig. 1(a)). The electric shear stress accelerates the liquid near the free surface, accelerating the bulk liquid from nearly zero velocity at the cone base to  $>10$  m/s at the cone apex. This operating mode is generally known as the cone-jet mode<sup>29</sup>. For a comprehensive review on the cone-jet electro spray, readers are referred to Ref. <sup>30,31</sup>.

We shall clarify the terms of printing and deposition. Printing suggests the process can pattern the materials on the substrate without the need of a mask, while deposition usually does not involve active patterning. Although this review is focused on printing photovoltaic devices, the principles and ideas are also applicable to printing of many types of thin film optoelectrical and semiconducting devices. Electro spray can provide both printing and deposition by positioning the substrate at different distance from the Taylor cone. When such distance is on the order of millimeter or is comparable with the cone diameter, it is termed as near-field and the jet has not broken up or the droplets have not diverged too much from the center line. Near-field is suitable for printing. When the substrate is centimeters away from the emitter, it is considered as far-field and the droplets have sufficient time to repel each other and from a plume to cover a circular area of a few millimeter to centimeters in diameter. Far-field is suitable for material deposition (Fig. 1(a)).

**Table 1 | Comparison of electro spray printed active layers of three different solar cells.**

Active layer	Perovskite	Polymer	DSSC
Solution	Newtonian	Non-Newtonian	Non-Newtonian (suspension)
Solute	Salt	Polymer	TiO <sub>2</sub> nanoparticles
Solvent	Polar (DMSO, DMF, ...)	Nonpolar (CB, DCB, OXY, ...)	Polar (Ethanol, EG, ...)
Electric conductivities	High (~1 S/m)	Low (~10 <sup>-5</sup> S/m)	Medium (~10 <sup>-4</sup> S/m)
Typical flow rate per source	40 μL/h	1000 μL/h	300 μL/h
Typical droplet size	<1 μm	~20 μm	~10 μm
Typical evaporation time	0.1 ms	10 ms	1 ms

(DMSO: dimethyl sulfoxide; DMF: *N,N*-dimethylformamide; DCB: dichlorobenzene; CB: chlorobenzene; OXY: o-xylene; EG: ethylene glycol)

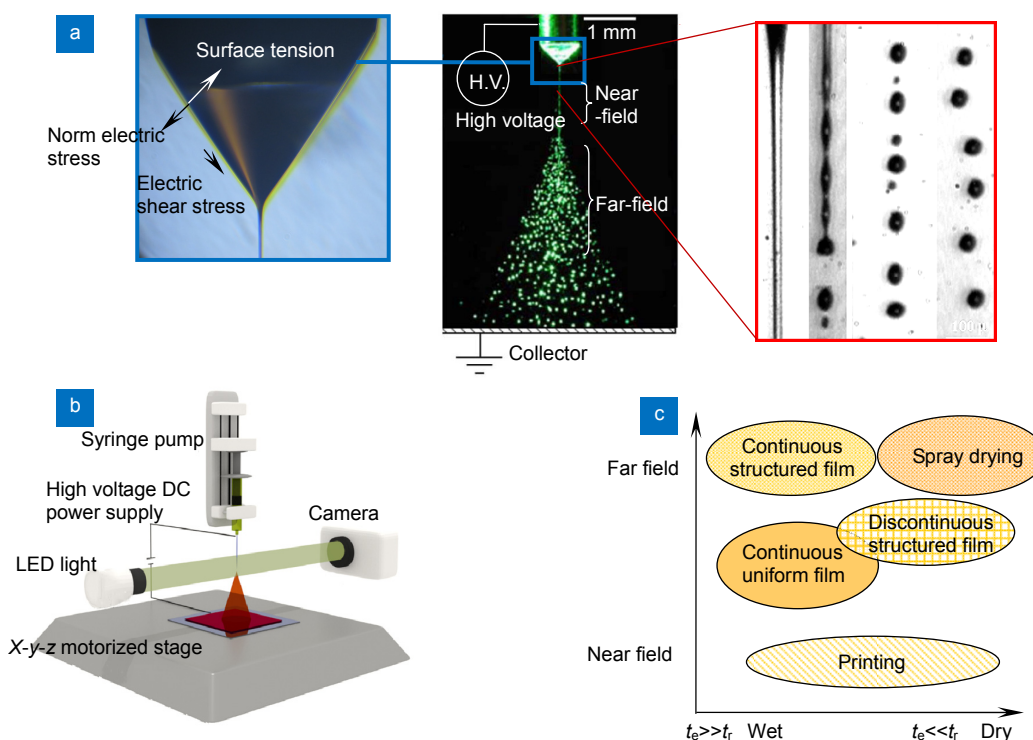


**Fig. 1 | The electro spray and electro spray as a tool for material processing. (a)** A close-up view of the Taylor cone with a fine jet attached to the cone, and the jet diameter is typically 10 to 10<sup>4</sup> nm, and details of the break-up process<sup>31</sup>. **(b)** A typical arrangement of the electro spray. **(c)** Several typical outcomes of using electro spray as a material processing tool.

Another aspect for material processing is the droplet evaporation. The solvent of the droplet will evaporate during the time it travels from the emitter to the substrate. For small droplets, such evaporation can happen very quickly (see the subsequent section). If there are still enough solvent left to keep the droplet fluidic upon impact on the substrate, we consider as “wet”. Otherwise it is considered “dry”. The combination of near-field, far-field, wet, or dry provide several possible outcomes of using electro spray as a material processing tool (Fig. 1(c)). One

can quantitatively estimate the traveling time and evaporation time, and hence design the process in advance for desirable results.

The cone-jet electro spray has the following properties uniquely suitable for making high performance SPPVs:

i) Quasi-monodispersity: The cone-jet mode has the useful characteristic of droplet size monodispersity<sup>32</sup>. Typical relative standard deviation (RSD) of the droplet diameter for the cone-jet electro spray is ~10%<sup>33</sup>. Uniform droplet size is beneficial for creating uniform mass and

heat flux upon interaction of the droplet with the substrate, in turn generating higher quality thin films. The uniform droplet size also enables the creation of homogeneous, ordered, or periodic structures. From the fundamental investigation point of view, the quasi-monodispersity simplifies modeling because the study of a single electrospray or even a single droplet can reveal valid insight for the entire spray.

ii) Tunable droplet and particle size in a wide range: For thin film PVs, small droplet size is essential because the active layer is typically merely 100 nm (polymer solar cells) or ~300 nm (perovskite). Moreover, tight control of the droplet diameter enables precise adjustment of the active layer thickness as well as the film morphology. As to be explained in the subsequent section, scaling law shows that by changing the flow rate or the liquid electric conductivity, a wide range of droplet sizes can be achieved. This is important to change the drying time, which will be discussed in the subsequent section.

iii) Robust process: The unique jetting mechanism of electrospray eliminates liquid/solid friction. Thus, compared to other techniques such as ink-jet printing (IJP), electrospray is a robust method to process liquids with high viscosity or with high solid contents. Especially for complex fluids, electrospray has the unmatched capability of producing sub-micrometer droplets with low risk of clogging.

iv) Dramatically reduced process time: Both the heat diffusion time and the evaporation time scale with the droplet diameter squared or  $d^2$ . A small decrease in  $d$  leads to dramatic reductions in the characteristic time<sup>34</sup>. Short heat diffusion time suggests rapid and precise regulation of droplet temperature, which is crucial during thin film fabrication processes. For heat-sensitive materials, as in polymer solar cells, it is possible to have a reasonably fast evaporation even at modest temperatures, which avoid thermal destruction to the material.

v) Improved deposition efficiency: When electrically charged droplet approaches a conducting surface, an image charge is induced, generating an additional Coulombic force which tends to prevent droplet rebound from the substrate<sup>26</sup>. This results in less material waste, and thus negative environmental impacts related to material waste is minimized.

#### Characteristic time of main processes in electrospray printing

Droplet evaporation and droplet travel are two main pro-

cesses prior to the droplet impact on the substrate, and the characteristic time describes the outcome of film forming mechanism: either by the overlapping of wet droplets, partially dried droplets, or dried spherical/nonspherical particles on the substrate. Consequently, the morphology of electrosprayed films is determined by the “wetness” or the degree of droplet evaporation prior to landing on the substrate. For example, for perovskite solar cells, it is desirable to make smooth film without pin-holes. Accordingly, the droplets should remain fluidic upon impacting the substrate, allowing neighbor sessile droplets to coalesce and collectively form a continuous wet film before solvent completely evaporates. For DSSC and certain polymer solar cells, it is beneficial for the droplet to dry completely before reaching the substrate to form discontinuous film of “nano grass”<sup>35</sup> or a porous film with many voids<sup>36,37</sup>.

To quantitatively analyze the processes, we denote  $t_r$  as the droplet residence time and  $t_e$  as the droplet evaporation time. Many parameters in the electrospray printing process will affect these  $t_r$  and  $t_e$ . The droplet diameter and electrical charge (or current) are the two most important characteristics of a cone-jet electrospray, and they are usually estimated from scaling laws. Several scaling laws have been introduced<sup>30,38</sup> and the consensus for the universal scaling laws has not been reached and is subject to debate and further investigation. It does seem reasonable to treat the liquid conductivity as the most important parameter to categorize the liquid as highly conducting and weakly conducting. One scaling law for droplet size is<sup>39</sup>:

$$d_0 = C_d \left( \frac{\rho_l \varepsilon_0 Q^3}{\gamma k} \right)^{1/6}, \quad (1)$$

where  $C_d$  is the scaling constant of roughly unity,  $\rho_l$  the solution density,  $\varepsilon_0$  the vacuum permittivity,  $Q$  the solution flow rate,  $\gamma$  the surface tension,  $k$  the electrical conductivity. Equation (1) suggests that  $Q$  and liquid properties (such as  $\gamma$  and  $k$ ) can be used to tune the droplet diameter. In addition, a more conductive liquid (high  $k$ ), such as an ionic liquid or liquid metal, can lead to submicrometer droplets and even individual ions<sup>30</sup>.

To the first order approximation,  $t_r$  is:

$$t_r = \frac{h}{u_t}, \quad (2)$$

here  $h$  is the gap between the emitter and the ground electrode, and  $u_t$  is the droplet terminal velocity. The

small droplet instantly reaches terminal velocity:

$$u_t = \frac{q_0 E}{3\pi\mu d_0} \quad (3)$$

where  $E$  is the electric field on the order of  $U/h$ , and  $\mu$  is the viscosity of the gas (mostly air or nitrogen),  $q_0$  is the electric charge of each droplet:

$$q_0 = \frac{I}{Q} \cdot \frac{\pi}{6} d_0^3 \quad (4)$$

The current  $I$  is inferred from the scaling laws<sup>39</sup>:

$$I = C_1 (\gamma k Q)^{1/2} \quad (5)$$

where  $C_1$  is another scaling constant. Therefore,  $t_r$  can be explicitly written from Equations (2) to (5).  $t_e$  is estimated from the  $d$ -squared law<sup>40</sup>:

$$t_e = \frac{d_0^2}{K_e(T)} \quad (6)$$

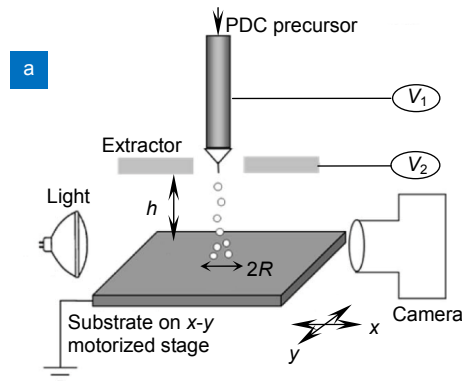
where  $T$  is the temperature, and  $K_e$  is the evaporation rate.  $K_e$  can be modeled from mass transfer principles based on an isolated droplet<sup>41</sup>:

$$K_e = 8D_{\text{diff}} \frac{\rho_g P_v}{\rho_1 P_0} \quad (7)$$

where  $D_{\text{diff}}$  is the mass diffusivity of vapor molecules to the ambient environment (typically air or nitrogen),  $\rho_g$  is the solvent vapor density,  $P_v/P_0$  is the ratio of vapor pressure of the solvent to ambient pressure. For nanometer-sized droplet, the evaporation rate can be corrected by the size effect, but such effect is negligible for most electro spray printing and deposition cases.

Combining Equations (1) to (7), and taking scaling constants from literature<sup>39</sup>, we write the ratio of resident time to evaporation time, where  $h$  is defined as the  $Da$  number:

$$Da = \frac{t_r}{t_e} = \left( \frac{8\sqrt{2}}{\epsilon_0^{2/3}} \right) (\gamma k)^{1/6} \left( \frac{h^2}{UQ^{3/2}} \right) \left( \frac{D_{\text{diff}} \mu \rho_g}{\rho_1^{5/3}} \right) \left( \frac{P_v}{P_0} \right) \quad (8)$$



From Equation (8), it is clear that:

i) Over 9 parameters ( $\gamma, k, h, U, Q, D_{\text{diff}}, \mu, \rho_g, P_v$ ), in the electro spray deposition process can affect the outcome of deposition or printing;

ii) Both conductivity and surface tension have weak effect on the ratio (1/6 power);

iii) The ratio is very sensitive to two parameters: emitter-substrate distance and flow rate;

iv) The ratio scales with solvent vapor pressure. It is worth pointing out that a common misunderstanding for organic solvents is that solvent with high boiling point is less volatile or evaporates more slowly. In fact, the volatility or evaporation rate of a solvent is not directly affected by the boiling point. Instead, Equation (7) suggests that  $K_e$  is proportional to solvent vapor pressure. In other word, solvents with low vapor pressures evaporate more slowly and correspond to smaller  $Da$ .

### Printing footprint

The width or diameter of the spray footprint is a basic parameter to determine the printing resolution and calculate the film thickness from mass conservation. Specifically:

$$\delta = \frac{Q\phi}{2RV} \quad (9)$$

where  $\delta$  is the film thickness,  $\phi$  is the volume concentration of the precursor,  $R$  is the radius of the footprint of a stationary spray, and  $V$  is the printing speed. Equation (9) is derived from mass conservation and the film thickness can be precisely determined.

Beside direct measurement of  $R$ , if an extractor configuration is adopted (Fig. 2(a)), one can use a simplified model for the spray expansion<sup>21</sup>. In such model, the spray is assumed to be continuous charged media and the volumetric charge density  $\rho_e$  is continuous. Due to the very

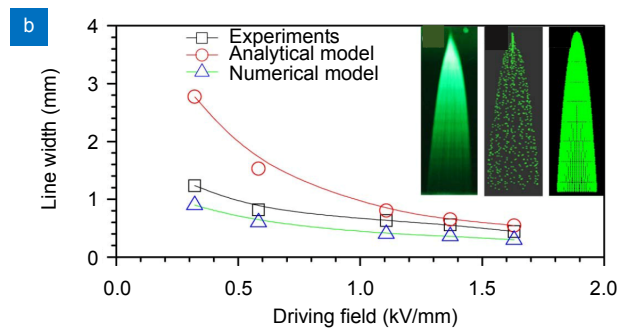


**Fig. 2 | (a)** Electro spray printing setup with three-electrode configuration (emitter, extractor, and ground). **(b)** Effect of driving field on line width. Inset: electro spray profile images from (left) experiments, (middle) Lagrangian model simulation, and (right) analytical model (Equation (12))<sup>21</sup>.

small droplet diameter, the droplet is assumed to reach terminal velocity  $u_t = qE / 3\pi\mu d_0$  instantly<sup>42</sup>. The electrical mobility of the charged droplet is defined as  $Z = q / 3\pi\mu d_0$ . With these assumptions and starting from the law of charge conservation, Ohm's law, and Gauss law, one can obtain:

$$\frac{Z}{\epsilon_0} \rho_e^2 + u \frac{d\rho_e}{dx} = 0 \quad (10)$$

The solution to Equation (10) is:

$$\frac{1}{\rho_e} - \frac{1}{\rho_{e,0}} = \frac{Z}{\epsilon_0 u} x \quad (11)$$

where  $\rho_{e,0} = \rho_e(x=0)$ . Immediately after the cone-jet breakup, the droplets are tightly aligned, making  $1/\rho_{e,0}$  negligible compared to  $1/\rho_e$ . On the other hand,  $\rho_e = I_0 / \pi R^2 u$ . Since  $\mathbf{u} = \mathbf{E} \cdot \mathbf{Z}$ , Equation (11) reduces to:

$$R = \left( \frac{I_0}{\epsilon_0 \pi E^2 Z} x \right)^{1/2} = \sqrt{x_R x} \quad (12)$$

and

$$x_R = \frac{I_0}{\epsilon_0 \pi E^2 Z} \quad (12)$$

Equation (12) suggests that the spray profile is parabolic and  $R$  is inversely proportional to the driving field. Combined with scaling laws of the current, one can also conclude that high flow rate and high conductivity usually lead to larger footprint deposition, while low flow rate and low conductivity are needed for high resolution printing (small  $R$ ). The separation  $x$  is also important. For small  $x$ , or near-field, the electro spray functions as printing; for large  $x$ , or far-field, the electro spray is more appropriate for deposition.

### Electric conductivity

The electrical conductivity  $k$  is a critical parameter because it determines the droplet diameter and film morphology. From the standpoint of solution properties, the three categories of solar cells represent three vastly different liquid systems: perovskite precursors has high concentration of ions dissolved in polar solvents, leading to extremely high liquid conductivities by electro spray standards; polymer solutions are often made from non-polar solutions that exhibit low conductivity, while DSSC solutions have medium conductivities because polar organic solvents involved.

The solvent needs to have sufficient electrical conductivity  $k$ . Here "sufficient" means it can satisfy Equation (1) in producing desired droplet size at tolerable flow rates. For polymer solar cells, the most commonly used solvents

for conjugated polymers are dichlorobenzene (DCB) and chlorobenzene (CB), which are non-polar and their electrical conductivities are too low to electro spray. To mitigate this issue, small amounts (up to ~20 vol.%) of additives can be mixed in the solution to increase the conductivity. Polar solvents are often used because they have certain concentration of dissociated ions at chemical equilibrium that provide the required conductivity. Examples of polar solvents include 1,1,2,2-tetrachloroethane (TCE)<sup>43</sup>, acetone<sup>44</sup>, dimethyl sulfoxide (DMSO), *N,N*-dimethylformamide (DMF), and acetonitrile<sup>45</sup>. The polarity of these solvents is relatively weak and the boost in electrical conductivity is modest. Therefore, trace amount of acetic acid, an organic ingredient with strong polarity, has been added to the bulk to boost conductivity for electro spray fabrication of solar cells<sup>46</sup>.

Equations (6) and (7) can be used to guide the design of solvent formula. Take electro spray printing of perovskite precursor for example. The typical flow rate is ~500 nL/min and  $k \sim 4$  S/m, and the initially  $d_0 \sim 150$  nm. The small droplets are prone to rapid evaporation according to Equation (6). To guarantee wet deposition,  $\gamma$ -Butyrolactone (GBL) and 1-Methyl-2-pyrrolidinone (NMP) could be used as the solvents, both have low vapor pressure (~200 Pa for GBL and ~40 Pa for NMP at 20 °C) to increase  $t_e$  to ~0.1 ms<sup>47</sup>.  $h$  is decreased to ~1 mm to reduce  $t_f$  so that  $t_f \leq t_e$ . Different ratios of  $t_f$  over  $t_e$  lead to different morphology of either nanoporous ( $t_f > t_e$ ) or dense perovskite film ( $t_f < t_e$ ), as shown in Figs. 10(a) and 10(b).

### Charged droplet impact on conducting surface

The basic event for printing or deposition based on liquid droplets is the impact of a single droplet on the solid and smooth substrate. Figure 3(a) shows a typical case of such event for the inkjet printing<sup>17</sup>. A small bubble is clearly visible after the droplet settles. The gas entrapment and bubble formation are very common for liquid droplet of wide size range, namely from sub-micrometer to millimeters. The mechanism of gas entrapment is the following. Immediately prior to the impact, the gas layer between the droplet and the solid substrate surface is as thin as few micrometers and a creeping gas flow forms and the gas pressure buildup  $P_b$  can be comparable with the surface tension.  $P_b$  can "dent" the liquid droplet and the thin layer of gas is entrapped by a circular contact line. To eliminate the gas entrapment, the droplet can be electrically charged. In fact, even modest charge levels can fundamentally change the outcome of the impacting event

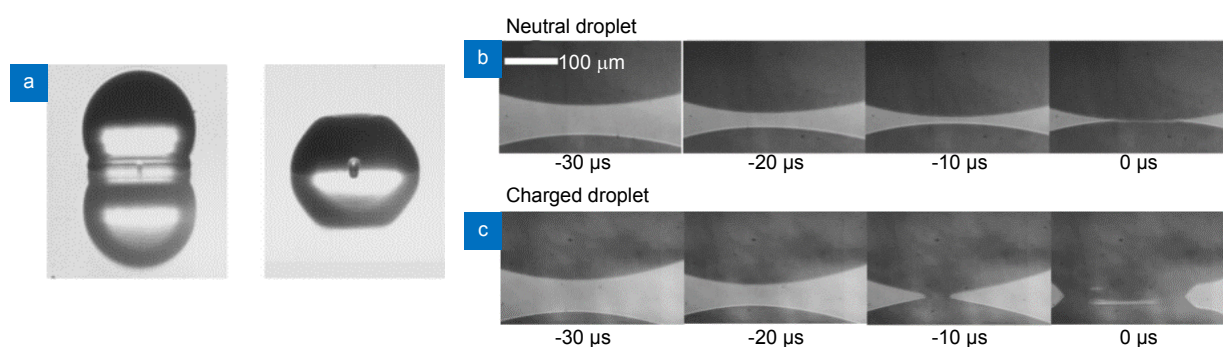


**Fig. 3 | The impact of a single droplet on the solid and smooth substrate for the inkjet printing<sup>17</sup>.** (a) Side-view of impact process of neutral and charged droplets on mirror-like ITO glass. (b) Neutral droplet and (c) droplet charged at 63 pC. Impacting velocity for both scenarios: 0.6 m/s, droplet radius: 1.25 mm<sup>48</sup>.

because the electric stress alters the air film structure (Fig. 3(b)). The electric stress overcomes gas pressure and promptly deforms the droplet bottom into a conical tip to make a center touchdown, forming a circular contact line moving outwards that does not trap any gas. Gao et al. further showed that the center touchdown happens when the charge level is above a critical value as low as  $\sim 1\%$  of the maximum charge the droplet can carry, a result due to the local surface charge intensification<sup>48</sup>. The finding provides new insights mitigating pinhole defects in printing. The liquids used in SPPV could be more complex, being either polymer solutions or metal oxide nanoparticle suspensions that are non-Newtonian. The impact processes of electrospay droplets of these liquids are of great interest and is worthy of further investigation. Nevertheless, electric charge brings another intrinsic advantage of electrospay potentially for mitigating pinhole defects in droplet-based additive manufacturing and improving printing quality.

### Multiplexed electrospay

The application of single electrospay in PV manufacturing is limited by the very low liquid flow rate passing the nozzle, as well as the small footprint (on the order of  $0.1 \text{ cm}^2$ ) that can be covered. It is indispensable to massively multiplex the electrospay to dramatically increase the throughput and the deposition area. Three common ways of multiplexing are linear arrays, multi-jet mode, and planar arrays. The linear array simply entails duplication of several capillaries operating in parallel such as etching of fused silica capillaries (Fig. 4(a))<sup>49</sup> or by micromachining. The multi-jet mode entails stabilizing a number of electrospays on the circumference of the tube outlet through which a common liquid is pumped. The multi-jet mode is based on the fact that when the electric field near the cone of the electrospay is sufficiently intense, the single

jet may split into two or more jets<sup>29</sup>. Ordinarily, such mode is rather unsteady and the range of flow rates within which appreciable multiplexing is achieved is small. Duby et al. reported on a novel approach which anchors the jets at discrete points around its perimeter through some sharp grooves precisely machined at the outlet of the atomizer (Fig. 4(b))<sup>50</sup>. The planar MES system is also extensively studied. To date, the highest packing density reported has reached  $1.1 \times 10^4 \text{ sources/cm}^2$ <sup>51</sup>. This system implemented silicon nozzles fabricated using tailored deep reactive ion etching (DRIE) process and adopted distributor-extractor-collector arrangement. The extractor electrode, which is separated from the electrospay nozzle array at a distance comparable to the inter-nozzle spacing, serves the dual function of limiting electrostatic interference between neighboring electrospay sources and electrostatically shielding Taylor cones from the space charge of the spray cloud. Ref.<sup>42</sup> reported a linear electrospay (LINES) system machined by a CNC platform with micrometer precision. Nozzle arrays based on plastic and metals polymers with packing densities of 20 sources/cm are achieved. Through numerical simulation, Yang et al.<sup>42</sup> has shown that the film is very rough if there is no any relative motion between the substrate and the 1D (linear) nozzle arrays. Once relative motion is introduced, the accumulated deposition becomes uniform.

### Practical aspects for electrospay printing

i) High voltage safety, power, and cost: The high voltage required in the electrospay should not be a severe concern for power, cost, or safety. The power consumption of the electrospay is quite low. The typical voltage for the electrospay is less than 10 kV, and the current drawn per electrospay is less than 100 nA. Therefore, the power consumption is  $\sim 1 \text{ mW/nozzle}$ . The low current will not

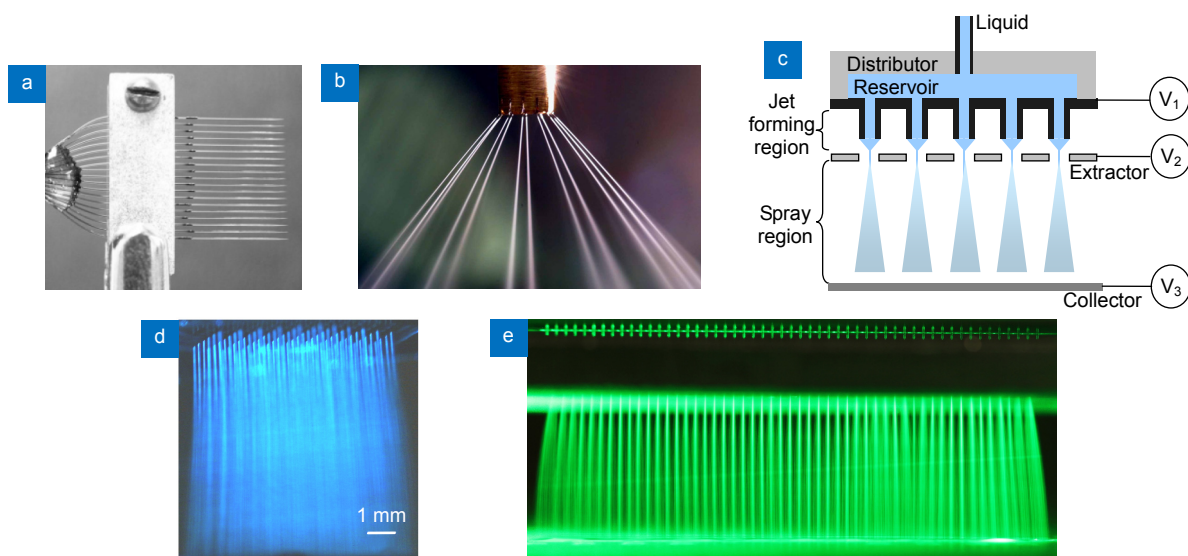


**Fig. 4 | Three typical configurations of multiplexed electrospray.** (a) Linear array of 19 silica capillaries<sup>49</sup>. (b) Multi-jet mode with 24 jets stabilized on the grooved nozzle<sup>50</sup>. (c) The three-electrode design<sup>51</sup>. (d) Planar array of silicon nozzles<sup>51</sup>. (e) CNC micromachined linear array made of brass<sup>42</sup>.

impose lethal hazard if a proper current limiting resistor is connected to the high voltage output. Miniaturized high voltage power supplies are commercially available or can be conveniently made based on a low-cost Cockcroft Walton multiplier.

ii) Cone visualization: The cone-jet is often challenging to visualize because of the small jet diameter size, which could be less than 1  $\mu\text{m}$ . The pulsing mode, which is an undesired operation mode due to the polydispersity and much larger droplets it generates, could be misidentified as cone-jet mode due to low magnification power of the microscope, insufficient camera frame rates or inappropriate illumination. Proper visualization equipment coupled with operation experience is critically important for ensuring good electrospray deposition results.

iii) Liquid supply: the stable operation of Taylor cone and reliable estimate of droplet diameter and current all depend on the accurate flow rate delivered to the Taylor cone. The most convenient way of supplying liquid is to use a syringe pump. Care needs to be taken especially at low flow rates. The dead volume should be as low as possible, the tubing should be rigid (metal, glass or at least hard plastics; avoid rubbery or elastic tubing). Gas bubbles in the fluid line should be avoided. The syringe wall and piston should be made of glass or inert materials such as Teflon. No lubricant shall be introduced. It is worth noticing that piston covered with the rubber gasket for sealing purpose is not suitable for many solvents such as DCB and CB, which will swell the rubber gasket. The choice of the size of syringe is also important because the

pump is driven by stepper motors, and its motion becomes intermittent at very low linear speed. This is the case when a large syringe is paired with very low flow rate, for example, 50 mL syringe running at 50  $\mu\text{L}/\text{h}$  requires 1000 hours to empty the syringe. A rule of thumb is to consume the volume of the syringe within an hour. For example, for the low flow rate of 50  $\mu\text{L}/\text{h}$ , a syringe size of  $\sim 50 \mu\text{L}$  is appropriate.

iv) Stabilization of Taylor cone: a stable Taylor cone is the necessary condition for establishing the fine liquid jet and efforts have to be made to stabilize the Taylor cone, especially at low flow rates. Beside the liquid supply, the emitter itself also bears importance in achieving stable Taylor cones. An ideal electrospray emitter should have these characteristics: (i) Large operation envelope in the  $Q$ - $U$  domain, meaning the Taylor cone can be established for a wide range of voltages and flow rates. (ii) Resistance to external disturbance including mechanical vibration, gas flow, fluctuations in flow supply, and nonstable wetting to the capillary. (iii) Robustness to clogging and damage. For those reasons, electrospray emitters tend to have very small tip diameter such as metal capillary emitter of 36 gauge (outer diameter of 110  $\mu\text{m}$ )<sup>52</sup> or glass capillary of 1 to 10  $\mu\text{m}$  in outer diameter. However, these fine emitters are delicate to handle, easy to clog, and high cost. Therefore, alternative Taylor cone stabilizing strategies have been presented, such as externally wetted solid tip<sup>53</sup>, pointed hypodermic needles<sup>54</sup>, and sharp inserts at the nozzle tip<sup>55,56</sup>. The emitter (typically a metal or glass capillary) surface is usually hydrophilic, and sometimes

the liquid tends to climb up the capillary, causing the flow rate going through the Taylor cone is not the value prescribed. The capillary flow also destabilizes the Taylor cones, sometimes even making it impossible. One can coat fluoropolymer on the emitter outer surface to make it hydrophobic and suppress the liquid climbing.

### Polymer solar cells fabricated by electrospray

Polymer solar cells have attracted extensive research interest recently and the efficiency has improved from <math><0.1\%</math><sup>57</sup> to >16%<sup>6-8</sup>. The most effective structure of polymer solar cells is the bulk heterojunction (BHJ)<sup>58</sup> which is based on bulk heterojunction interpenetrating networks by blending donor and acceptor materials together. BHJ has a large-scale donor and acceptor interface area and hence an efficient photogenerated charge separation. The majority of studies on electrospayed solar cells are based on poly(3-hexylthiophene) (P3HT), which serves as a benchmark material because it is a classic and well-studied P-type conjugated polymer. P3HT and newer conjugated polymers such as PTB7 assemble intrinsically in anisotropic fashion<sup>59,60</sup>. Such anisotropy leads to dramatically different charge carrier mobilities along different orientations. The charge carrier mobilities are key figure of merits for investigation of electrospay-fabricated solar cells.

Kim et al. firstly used electrospay to fabricate PSCs with blended P3HT and PCBM as active layers<sup>44</sup>. They choose the mixture of 1,1,2,2-tetrachloroethane (TCE) and CB as the solvents to achieve stable atomization in the electrospay process. Three post treatments are pro-

posed: thermal annealing (TA), solvent vapor soaking (SVS), and SVS followed by TA. The performance of active layer films and PSCs are shown to depend upon the post treatment used. Absorption spectra and GIXRD spectra showed that the nanomorphology characterization of the ES-OPVs was similar with that of the SC-OPVs. However, the efficiency of the ES-OPV is still lower than that of spin-coated OPVs, although PCE is improved after these post-treatments for both electrospay and spin-coating method. One possible explanation for the less than expected efficiency is the boundary formed by the sequential piling up of pancakes, i.e., coffee-ring footprints generated from individual droplet impact on the substrate (Fig. 5(a)). The boundary between pancakes introduces resistance for the charge to flow, therefore it is likely that this pancake-morphology blocks the charge transport. Though the height between the boundary and the center of the pancakes was reduced during the TA, the shape of the pancakes remained intact (Fig. 5(c)). However, during the SVS treatment, i.e., the P3HT/PCBM films were subjected to saturated CB vapor at room temperature, the pancake boundaries disappeared prominently and a continuous film was formed (Fig. 5(b)). During the treatment of SVS followed by TA, the roughness of the film was further reduced (Fig. 5(d)). AC impedance ( $R_s$ ) spectroscopy further supported these authors' hypothesis: the  $R_s$  was reduced from 3.1 k $\Omega$  (TA-only) to 57  $\Omega$  (SVS/TA-treated). The reduction in boundary densities leads to enhanced charge transport and improved PCEs of the electrospayed OPVs. Although these authors presented a compelling case, the lower efficiency of the ES-OPV might be due to operation

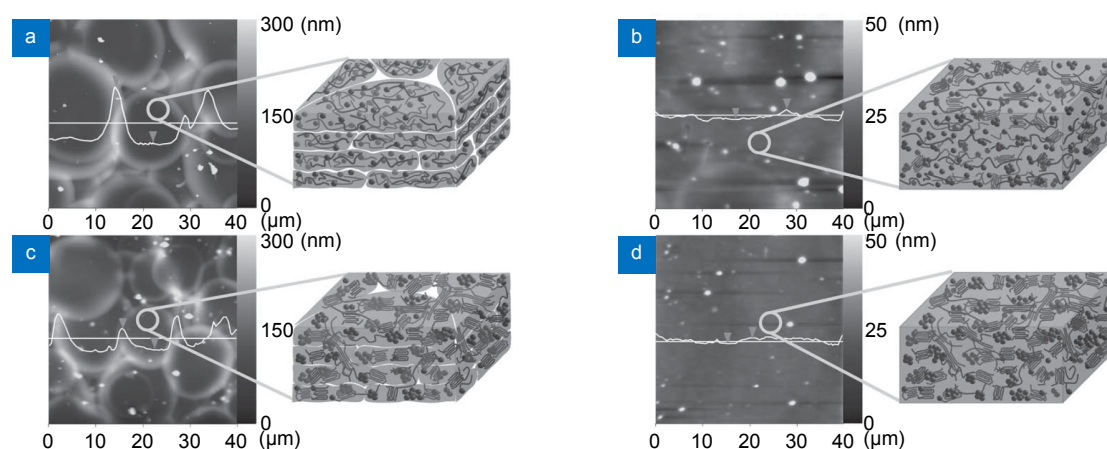


**Fig. 5 | AFM images of the electrospayed P3HT/PCBM-blend films on the PEDOT/PSS-coated ITO/glass. (a) As-cast. (b) Solvent vapor soaking (SVS). (c) Thermal annealing (TA), and (d) SVS followed by TA. The white line on the AFM images are the cross-section height. The cartoons are schematic illustrations of the P3HT/PCBM morphologies, depicting the nanoscale phase transition of P3HT (wires) and PCBM (balls) as well as the pancake boundary<sup>44</sup>.**

of the electrospray at less-than-ideal conditions. The diameter of the solid pancake (Fig. 5(a)) appears quite large ( $>15\ \mu\text{m}$ ), which suggests the unevaporated liquid phase droplet precursor may be as large as  $100\ \mu\text{m}$ . It seems that the electrospray was operated in the undesired pulsing mode creating larger and more polydisperse droplets instead of the desired cone-jet mode which leads to much finer and more monodisperse droplet diameter.

Fukuda et al. investigated the relationship between the concentration of the solvent mixture (o-dichlorobenzene (o-DCB)/acetone) in the electrospray process and the surface roughness of the P3HT/PCBM blend thin film<sup>45</sup>. P3HT and PCBM were dissolved in o-DCB solvent and acetone was added into the solution with four concentrations: 5, 10, 15, and 20 vol%. The PSC fabricated by the solution with 20 vol% acetone exhibited the best photovoltaic metrics:  $J_{\text{sc}}=7.44\ \text{mA}/\text{cm}^2$ ,  $V_{\text{oc}}=0.57\ \text{V}$ ,  $\text{FF}=45\%$ , and  $\text{PCE}=1.9\%$ . In contrast, PSCs fabricated by the solution with 10% acetone had extremely low  $J_{\text{sc}}$  ( $<10\ \mu\text{A}/\text{cm}^2$ ) and  $\text{PCE}$  ( $<0.001\%$ ). These authors argued that PSCs with smoother active layer surface morphology have higher efficiencies. The AFM images of the active layers fabricated by electrospray deposition with different concentrations of acetone were shown in Fig. 6. The root mean square (RMS), which represents the roughness of the P3HT:PCBM layer, is less for 5 and 20 vol% acetone additive than those with 10 and 15 vol%. The droplet diameter increases as the concentration of acetone is increased. Therefore, the 5 vol% acetone solution resulted in finer droplets and smoother surface than that of 15%. However, the low roughness of 20 vol% acetone remains unsatisfactorily explained.

To optimize the solvent system and explore the route to

improve performance of the ES printed OPVs, Zhao et al. investigated and compared the morphology of P3HT:PC<sub>61</sub>BM (6,6-phenyl C61-butyric acid methyl ester) active layers deposited using electrospray with various additives as conductivity booster<sup>46</sup>. Compared with acetone and acetonitrile, the active layer formed by ES solvent doped with acetic acid demonstrated enhanced vertical segregation distribution, stronger light absorption as well as XRD intensity, leading to best PCE (3.02%) that is comparable to that of the OPV device fabricated by spin coating in  $\text{N}_2$  (3.13%). However, the photocurrent of OPV devices fabricated by electrospray was lower than that of spin coated devices, possibly due to the overlap of circular boundaries that retards the carrier transport.

Zhao et al. further clarified the interplay of nine independent parameters involved in an electrospray process, and the combined effect on morphology of active layers as well as device performance<sup>23</sup>. This work reduced the parameter space and captured the essence of the electrospray processes using the Damköhler ( $Da$ ) number of evaporation.  $Da$  (equation (8)) links 9 parameters, and small  $Da$  resulted ambiguous boundaries between the circular residues and more continuous films with smoother surface (Figs. 7(a-c)). Small  $Da$  also lead to enhanced optical absorption and P3HT crystallinity due to a higher order in the  $\pi$ - $\pi^*$  conjugated structure. Moreover, small  $Da$  may lead to less traps between P3HT and PCBM molecules and pinholes. Mostly remarkably, the carrier mobility exhibits monotonically dependence on  $Da$  values (Fig. 7(f)). This result suggests that  $Da$  is useful for simplifying the analysis for choosing appropriate operating parameters for electrospray deposition of polymer solar cells.

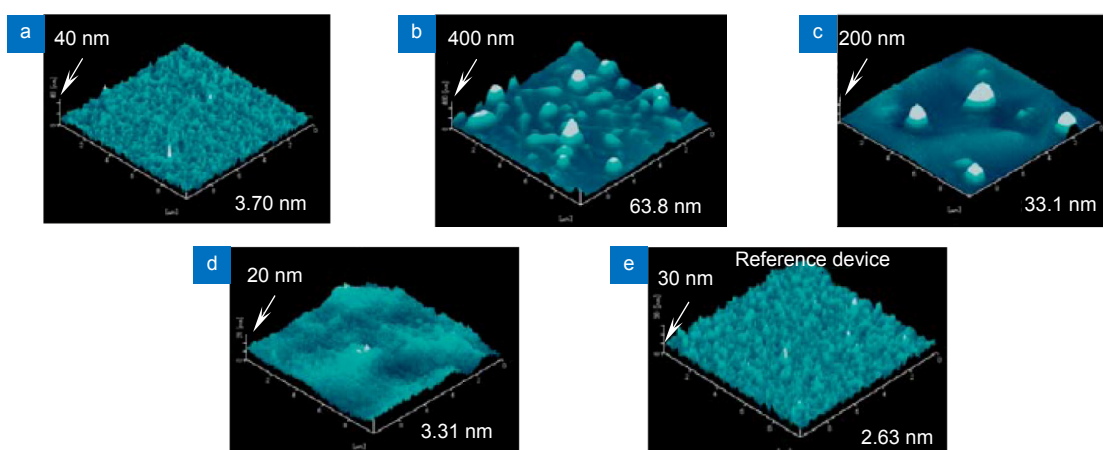
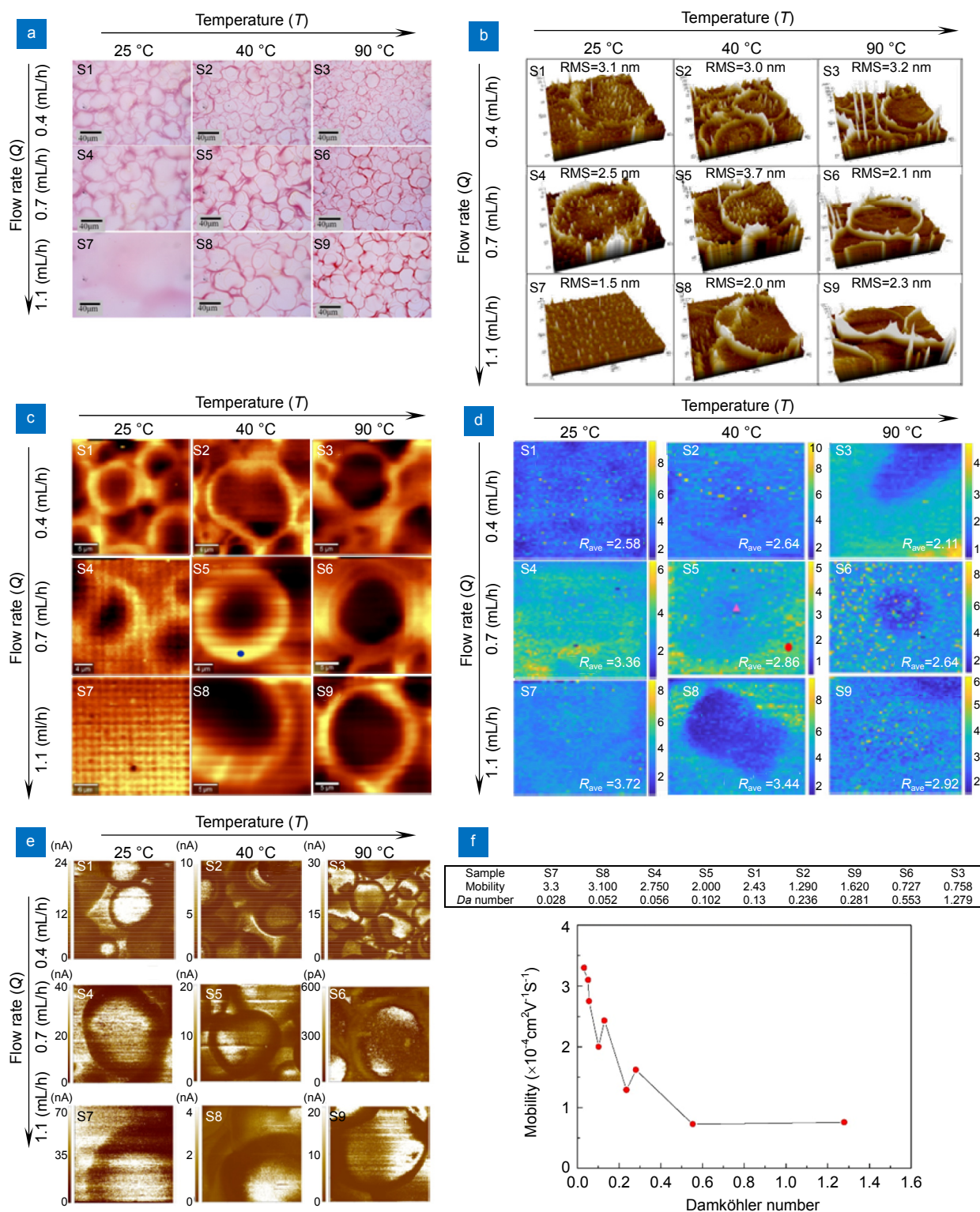


Fig. 6 | AFM image of the P3HT: PCBM layer. Acetone concentrations<sup>45</sup>. (a) 5, (b) 10, (c) 15, and (d) 20 vol%. (e) Reference device.

Zhao et al. studied the relationship between the nanoscale morphology and electrical properties of electrospay deposited films by characterizing both the resi-

dues of single droplets and thin films from the overlapping of multiple droplets<sup>22</sup>. The distribution of the P3HT aggregation states was analyzed by fitting the C=C mode



**Fig. 7 | Surface morphology of continuous thin films by electrospay at various flow rates and substrate temperatures (thickness of thin films is ~200 nm)<sup>22</sup>. (a) Optical microscopy images. (b) AFM images. (c) Raman intensity distribution. (d) Ratio images of Lorentzian components (R) derived from the Raman spectra,  $R_{\text{ave}}$ : average R value. (e) Current density map by C-AFM and (f) carrier mobility vs. Da numbers.**

of P3HT with Lorentzian functions (Fig. 7(d)). The conductive atomic force microscopy (C-AFM) was used to quantify local currents and depict the correlation between the nanostructure and charge-transport mobility (Fig. 7(e)). Both surface morphology and aggregation of the P3HT were found to strongly depend on the overlapping boundaries formed by the dry residues of individual droplets. Boundaries exhibit much higher charge-transport resistance and lower current. Thin films deposited with less droplet evaporation exhibit more homogenous morphology, more uniform phase segregation, and consequently higher charge mobility.

As we previously mentioned, the anisotropy nature of the P-type conjugated polymers leads to drastically different charge carrier mobilities measured along different orientations. For example, spin casted thin films of P3HT exhibit mobility of  $\sim 0.1 \text{ cm}^2/(\text{V}\cdot\text{s})$  in the plane of the film, but  $\sim 10^{-4} \text{ cm}^2/(\text{V}\cdot\text{s})$  in the direction perpendicular to the plane<sup>61</sup>. Low charge carrier mobility leads to slow carrier extraction, build-up of carriers and increased recombination rates, thereby decreasing PCE<sup>62</sup>. To increase mobility

in OPVs, reorientation of the polymer chain stacking direction by nanoimprint lithography<sup>63</sup> or polymer confinement within nanostructured templates<sup>64</sup> has been successfully demonstrated. A common theme among these polymer chain reorientation strategies is utilize additional polymer-solid interfaces oriented normal to the film plane, which effectively rotate the preferred orientation to be parallel to the film plane<sup>64</sup>. In principle, a polymer-gas interface should also be able to provide a similar function to re-orient the polymer chain alignment.

To investigate the polymer-gas interface's effect on orientation and alignment, Zhao et al. fabricated P3HT films with different residence time by varying  $h$ , which is the distance between the substrate and the emitter<sup>35</sup>. The SEM images (Fig. 8(a-d)) showed that as  $h$  gradually increases, the deposition outcome changes from overlapping of circular discs to nanopillars or "nanograss". The mechanism of the nanopillar formation is Coulombic fission, that is, the electric charge of an evaporating droplet remains the same. As the droplet diameter decreases, the electric repulsion stress increases and can overcome

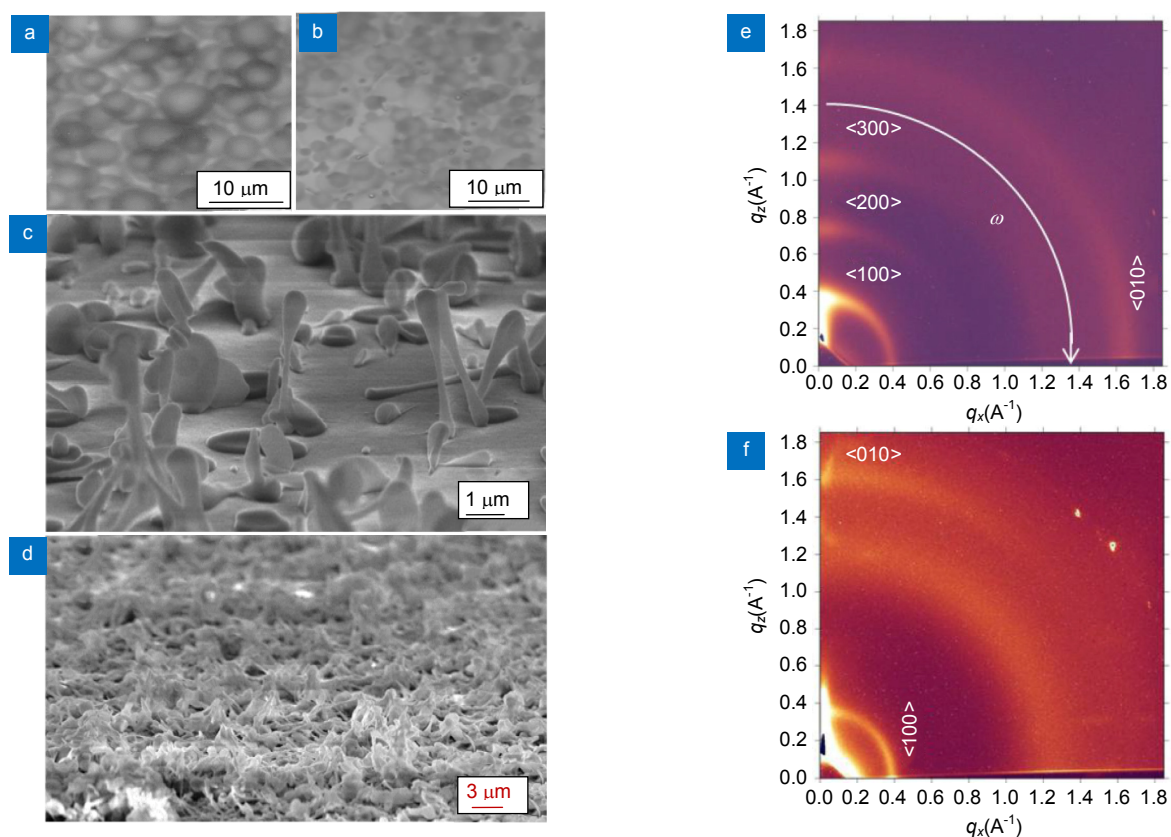


**Fig. 8 | SEM images of electrospayed P3HT films fabricated with different  $h$ .** (a) Low deposition density at 15.9 mm. (b) 19.6 mm and (c) 23.2 mm. (d) High deposition density at 23.2 mm. (e) GIXRD plot of a spin-cast P3HT film. (f) GIXRD of electrospayed P3HT film for  $h = 23.2$  mm<sup>35</sup>.

the surface tension to cause the droplet elongation. Meanwhile, the polymer concentration could be sufficiently high for entanglement that keeps the elongated shape in dried particles. Another notable feature is electric field polarizes and aligns the nanopillars along its direction and deposit perpendicularly to the substrate. The orientation of the polymer chain alignment was investigated by grazing incidence X-ray diffraction (GIXRD). GIXRD results of a spin-cast P3HT reference film (Fig. 8(e)) suggests an edge-on orientation. The comparison of Fig. 8(e) to Fig. 8(f) suggests a clear difference in the position of the high intensity peaks corresponding to  $\langle 100 \rangle$  (lamellar) and  $\langle 010 \rangle$  ( $\pi$ - $\pi$ ). In the electrospayed films (Fig. 8(f)) the lamellar peak is on the  $q_x$  axis and the  $\pi$ - $\pi$  peak on the  $q_z$  axis. Such shift suggests a drastic change in the overall crystal orientation of the electrospayed P3HT films.

Several attempts have been made on co-deposition method, new material systems, green solvents as well as new device architecture for ES-OPVs<sup>65–70</sup>. Fukuda et al. have attempted an alternative intermittent electrospay co-deposition method for two solutions of P3HT and PCBM, which were alternatively deposited with adjustable ratio by using high voltage pulse of variable pulse width<sup>65</sup>. The P3HT molecular ordering was comparable to that from spin-coated devices as suggested by Raman spectroscopy and GIWAX. The two layered BHJ device exhibits a maximum PCE of 3.1%, which is 40% higher than that of the uniformly mixed bulk heterojunction device due to higher carrier-collection efficiency. This author performed the first in situ measurement of solvent evaporation time by placing a CCD camera under the substrate in electrospay deposition<sup>66</sup>. They adjust the evaporation time by changing the applied voltage and switching solvents. They found long solvent evaporation

time leads to high crystallinity of P3HT with higher portion of P3HT crystallinity in edge-on orientation. They also studied the newer system of PTB7-Th:PC71BM blend by electrospay<sup>67</sup>. They also found that the crystal line grain size could be controlled by the solvent evaporation time. Both the crystallite size and PCE increased as the solvent evaporation time increased. The highest PCE of 8.6% was achieved. Takahira et al. made the contribution of using a non-halogenated solvent, o-xylene. They discovered that the addition of acetonitrile and 1,8-diiodooctane drastically reduced domain size of the organic active layer, resulting in improved device performance<sup>68</sup>. Khanum et al. used a single-step fabrication of porous photonic structure array with submicron feature size through electrospaying<sup>69</sup>. They found that this uniform periodic topography improved light scattering and enhanced light absorption. Although the authors showed an 18% increase in  $J_{SC}$  with the photonic structure compared to the planar reference, the mechanism of how the highly ordered porous photonic structure forms remains unclear and is subject to further investigation. Kimoto et al. used electrospay to fabricate double-layered (P3HT and PC<sub>70</sub>BM) and triple-layered (P3HT, interlayer, and PC<sub>70</sub>BM) OPV devices<sup>70</sup>. Although the highest PCE reported is only 1.45%, the work demonstrates the promise and unique capability of electrospay in fabricating multi-layer devices, and higher PCE can be expected for new polymers and NFAs.

## Perovskite solar cells fabricated by electrospay

The literature on perovskite PVs fabricated electrospay is considerably less than that on polymer electrospay, perhaps because the subject of perovskite PV is relatively new.

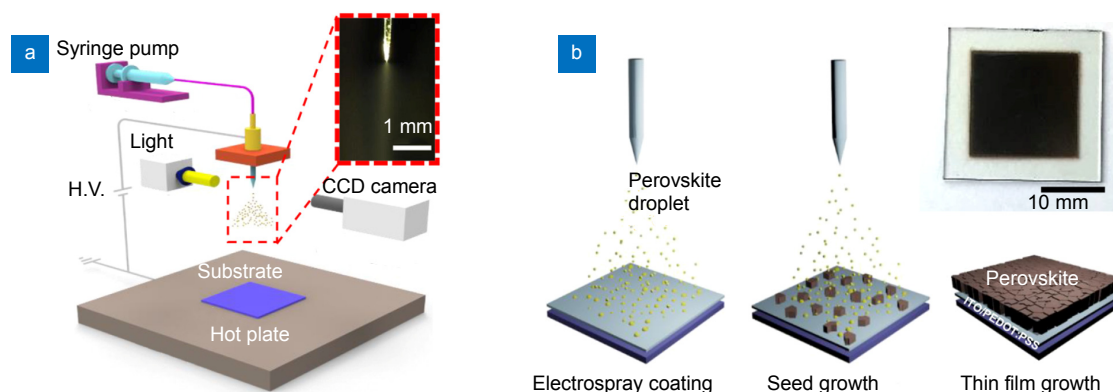


**Fig. 9** | Schematics of (a) electrospay deposition setup, and (b) the formation of perovskite films by electrospay deposition<sup>71</sup>. The inset photographs show the cone-jet and perovskite film.

Hong et al. claimed that the size of  $\text{CH}_3\text{NH}_3\text{PbI}_3$  precursor droplets can be systematically changed by modulating the applied electrical potential<sup>71</sup>. They have obtained pinhole-free and large grain-sized perovskite solar cells, yielding the best PCE of 13.27% with little photocurrent hysteresis. Their data demonstrate high reproducibility in PCE. The authors also showed continuous device fabrication by stop-and-go and nonstop movements. For nonstop movements, perovskite films were coated by electro spray on substrates of 25 mm  $\times$  100 mm at a speed of  $\sim$ 0.2 mm/s. Their work shows the promise of a low-cost continuous method for efficient perovskite photovoltaics by electro spray.

Lin et al. proposed a fabrication route combining electro spray with the solid-state reaction. This process belongs to the far-field spray drying regime in Fig. 1(c). They used electro spray to deposit the dried crystal precursors to study the transition of forming orthorhombic

$\text{CH}_3\text{NH}_3\text{PbI}_3$  films for perovskite solar cells<sup>72</sup>. The electro sprayed dry crystal precursors suppress the de-wetting of the perovskite film. Careful choices of the electro spray voltage lead to crystal precursors of appropriate dimensions, functioning as the solid-state reactants for the halogen exchange and facilitating a uniformly covered film after annealing. PCE of devices fabricated by this way is 9.3%. The optimization of the size and density of precursor particles, the de-wetting phenomena, as well as the detailed solid-state reaction mechanism are all worthy of further investigation. Kavadiya et al. studied the two-step method for perovskite films by electro sprays. They achieved PCE of 12% together with improved device stability with electro sprayed perovskite film over the spin-coated counterparts<sup>73</sup>. The electro spray method was also combined with other technology to prepare the absorber material of perovskite solar cells. The hybrid electro spray and vapor-assisted solution technology (VAST)

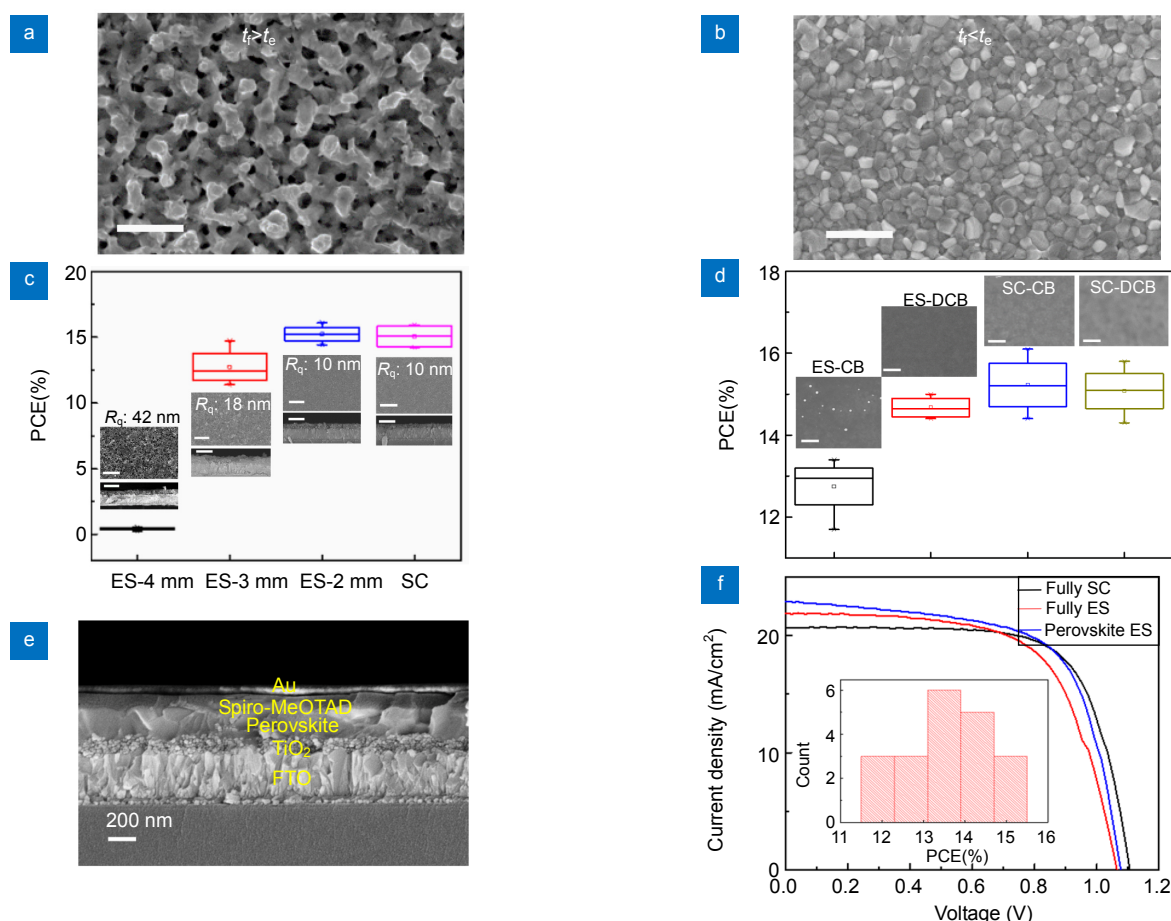


**Fig. 10** | Top-view SEM images of electro spray printed film when (a)  $t_f > t_e$  and (b) when  $t_f < t_e$ ; the scale bar is 1 micron. (c) PCE of electro spray printed and spin-coated devices. Inset: top-view and cross-sectional SEM images of  $\text{TiO}_2$  films electro spray printed at  $h=4, 3, 2$  mm and spin-coated. Scale bar: 600 nm. (d) PCE of perovskite solar cells by 4 fabrication conditions for Spiro-MeOTAD: electro sprayed with CB or DCB, and spin-coating with CB or DCB. Inset is the corresponding top-view SEM images. Scale bar: 400 nm. (e) Cross-section view SEM image of an all electro spray printed photovoltaic device. (f)  $J$ - $V$  curves of the champion cell of the all-printed, all spin-coated devices and the device with only perovskite layer electro spray printed. Inset: PCE histogram of all-electro spray printed devices<sup>47</sup>.

were used together to improve the efficiency of perovskite solar cells and achieved PCE of 10.74%<sup>74</sup>. High-throughput sheath-gas was adopted to assist electro-spray to obtain high-quality perovskite film and PCE of 14.2% was reached<sup>75</sup>.

Jiang et al. used electro-spray to print three functional layers (ETL, perovskite, and HTL) based on the architecture of FTO/TiO<sub>2</sub>/FA<sub>0.85</sub>MA<sub>0.15</sub>PbI<sub>2.85</sub>Br<sub>0.15</sub>/Spiro-OMeTAD/Au<sup>47</sup>. In printing each layer, the principle of wet film is followed. That is, to ensure  $t_e$  is longer than  $t_r$ . Strategies for achieving this requirement is different for each layer. Namely, for ETL, the primary strategy is to decrease residence time by reducing working distance  $h$ . This is because the choice of non-volatile solvent is prohibited as the TiO<sub>2</sub> nanoparticles were pre-dispersed in DI water and the addition of non-aqueous solvents destabilize the suspension. With short  $h$ , the electro-spray printed TiO<sub>2</sub> layer is indistinguishable from the spin-coated ones suggested by SEM images and  $J$ - $V$  curves. For the HTL, in formulating the Spiro-MeOTAD solution, DCB instead of CB is chosen due to the vapor pressure difference (~200 Pa for DCB and ~1600 Pa for CB at 25 °C). Therefore, DCB droplet has longer  $t_e$  to avoid complete evaporation and enable wet deposition (inset of Fig. 10(d)). For the perovskite layer, the authors mixed solvents with low vapor pressure and reduced the emitter/substrate distance at the same time. The device SEM image (Fig. 10(e)) shows the ETL, perovskite, and HTL are dense and uniform. Fig. 10(f) shows the  $J$ - $V$  curves of the champion cell of all-electrosprayed devices, all-spin devices, and devices with only perovskite layer electro-sprayed. The all electro-spray printed device showed  $V_{OC}$ =1.06 V,  $J_{SC}$ =21.9 mA/cm<sup>2</sup>, FF=64.1% and PCE of 15.0%, reflecting a modest performance drop from devices by spin coating.

Prior investigations<sup>12,76–78</sup> have shown the promise in the scalable fabrication of high-performance perovskite films, enabling PCE up to 20%. However, only a handful works applied the scalable process for all three functional layers<sup>15,79–81</sup>. Especially for devices with high PCEs, they still use spin coating<sup>77</sup> or evaporation<sup>12,76</sup> for ETL and HTL. The PCE of the all electro-spray printed champion cell in Ref.<sup>47</sup> is the highest for perovskite solar cells with all three functional layers made by scalable methods in air and at temperature < 150 °C (Table 2).

## Electrospray route for DSSC

Dye Sensitized Solar Cells (DSSC)<sup>86–90</sup> have good long-term stability<sup>91</sup> and decent PCEs reaching 14.3%<sup>92</sup>, which is the highest among organic solar cells before the NFA is introduced. In DSSCs, TiO<sub>2</sub> based photo-electrode film is responsible for light absorption and charge carrier separation/collection. Methods of fabricating TiO<sub>2</sub> layer include spin-coating<sup>86–88</sup>, screen-printing<sup>86,89</sup>, spray-coating<sup>93</sup> and blade-coating<sup>94</sup>. Readers are referred to some excellent reviews<sup>95,96</sup> for the characteristics of those methods.

The electro-spray deposits one droplet a time on the substrate. Each droplet from the electro-spray may contain none, single, or a few TiO<sub>2</sub> particles, depending on the particle concentration. Such discrete deposition enables forming of sub-structure within the film, which is typically not achievable by continuous phase methods such as spin coating or slot die coating. Electro-spray is a simple method to prepare the nano-sized spheres of photo-electrode nanoclusters (TiO<sub>2</sub>, ZnO or SnO<sub>2</sub>) with the advantage of removing synthesis steps of conventional sol-gel methods. Most works on ES-fabricated DSSCs reported so far show higher performance compared to

**Table 2 | Overview of PCE of the reported PSCs with all three layers (ETL, perovskite, and HTL) fabricated using scalable method<sup>47</sup>.**

Scalable method	Special conditions*	Best PCE	References
Infiltration	\	12.8%	[82]
Brush printing	\	9.1%	[83]
Slot-die	\	12.6%	[84]
Doctor blade	Humidity controlled (15%-25%)	10.7%	[80]
Slot-die	\	12.0%	[79]
Slot-die	\	14.7%	[81]
Screen-printing	High-temperature (500 °C)	13.3%	[85]
Blow drying	High-temperature (450 °C), glove box	17%	[24]
Electrospray printing	\	15.0%	[47]

\*Special conditions refer to: humidity control, environment control and temperature. The omission of a certain condition means it is not required during the preparation of PSCs.

cells fabricated by conventional methods, such as screen-printing or doctor-blading. The improved performance of ES-DSSCs were mostly attributed to the special morphology of the TiO<sub>2</sub> electrode fabricated by ES, which shows semi-self-assembled structure. Fujimoto et al. reported DSSCs fabricated by electro spray that exhibited a short circuit current,  $I_{SC}$ , higher than DSSCs prepared by conventional coating methods<sup>97</sup>. The increase in  $I_{SC}$  was attributed to TiO<sub>2</sub> needle bundles formed during the electro spray deposition process, which created an organized and enhanced ion path, increasing ion diffusion normally hindered by spherical TiO<sub>2</sub> particle structures. Zhang et al. reported increased open circuit voltage  $V_{OC}$  by introducing monoethanolamine (MEA) into precursor solution for electro spray<sup>98</sup>. They ascribed the change of  $V_{OC}$  to the different states of the TiO<sub>2</sub> nanoparticle obtained through controlling the size of TiO<sub>2</sub> particles. By adjusting the concentration of MEA, they effectively designed the electro spray solution and were able to control the TiO<sub>2</sub> film structure. The nanoporous structure

of the ES-fabricated TiO<sub>2</sub> can be locally modified by SHI post-treatment<sup>99</sup>. The high energy SHI process fused the nano-aggregated TiO<sub>2</sub> particles and formed a dense TiO<sub>2</sub>/FTO interface, which created an organized and enhanced ion path, enhancing electron transport through blocking the electron recombination.

Zero dimensional (0-D) hierarchically-structured TiO<sub>2</sub> (HS-TiO<sub>2</sub>) are considered as effective photo layer because of the benefits of large surface area for dye adsorption, rapid electron transport at reduced grain boundaries, and strong light scattering due to nanostructures<sup>96,100-103</sup>. Hwang et al. successfully demonstrated HS-TiO<sub>2</sub> spherical clusters of 200 to 1000 nm with electro spray and reported PCE up to 10.57%<sup>100</sup>. The schematic diagram of electro spray and the formation of HS-TiO<sub>2</sub> nanospheres were illustrated in Fig. 11. When proper electrical field was applied, spherical cluster of TiO<sub>2</sub> nanoparticles (termed by “HS-TiO<sub>2</sub> spheres”) are formed (Fig. 11, Figs. 12(d) and 12(e)), which were apparently different from the non-structured surface (Fig. 12(c)) produced using paste

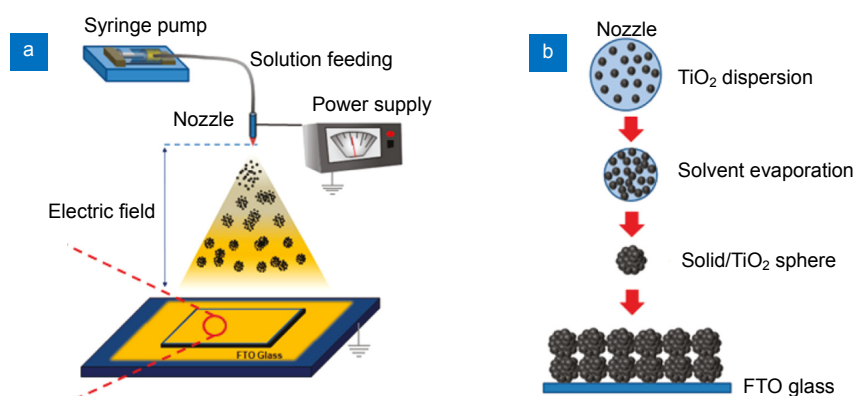


Fig. 11 | Schematic diagram of (a) electrostatic spray and (b) formation of hierarchically structured TiO<sub>2</sub> nanospheres<sup>100</sup>.

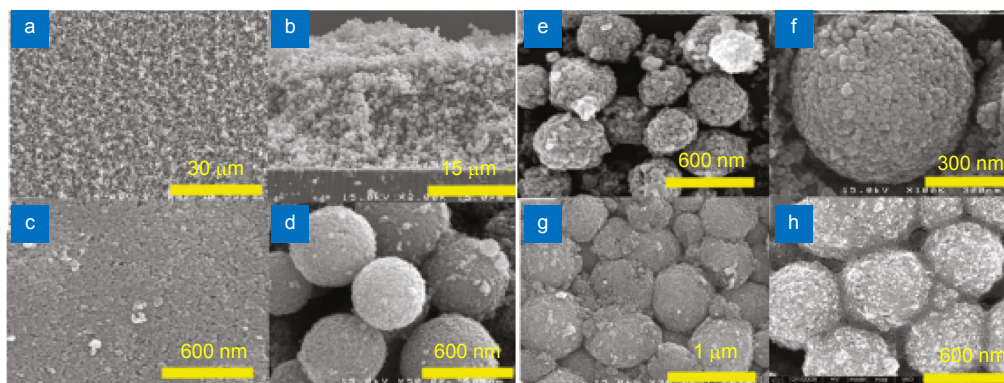


Fig. 12 | SEM images of (a) crack-free photoelectrode of HS TiO<sub>2</sub> spheres, (b) cross-sectional image of the HS-TiO<sub>2</sub> layer, (c) the non-structured TiO<sub>2</sub> layer by electro spray. (d) HS-TiO<sub>2</sub> with diameter of 640 nm. (e) HS-TiO<sub>2</sub> with diameter of 260 nm. (f) A HS-TiO<sub>2</sub> of nanoclusters of P25. (g) After heat treatment at 120 °C (for 10 min), and (h) post-treated HS-TiO<sub>2</sub> layer with TiCl<sub>4</sub> aq. solution<sup>100</sup>.

methods. The different sphere sizes (Fig. 12(d) and 12(e)) were obtained by varying the TiO<sub>2</sub> concentration. The authors believe that the ultrafast evaporation of solvent lead to the solid spherical TiO<sub>2</sub> clusters because a relatively high vapor pressure was formed at the surface of the monodispersed droplets containing TiO<sub>2</sub> nanoparticles. Moreover, the HS-TiO<sub>2</sub> spheres form mesopores, which improved the electrolyte absorption.

Better morphology is also observed in ZnO-based DSSCs fabricated by ES. As shown in Fig. 13, both films fabricated by electro spray and doctor-blading methods consisted of a three-dimensional network of interconnected particles<sup>104</sup>. However, in the doctor-blade film, the aggregation of ZnO nanoparticles occurred due to increasing crystallization at high sintering temperature. The average diameter of aggregated ZnO particles was ca. 95 nm (Fig. 13(a)). In contrast, almost no aggregation was observed in the ES-processed film and the ZnO nanoparticles were interconnected with smaller particle size of ca. 65 nm (Fig. 13(b)). The superior porosity of film prepared by electro spray benefited the dye-adsorption and electrolyte infiltration. The fine morphology of the ES-deposited film was partially attributed to the addition of PVA, which prevented agglomeration of ZnO during the high temperature calcinations process.

Besides fabrication of photo-electrodes, the electro spray method is also used in the dye soaking process for DSSC. Hong et al found that a quick solvent (ethanol) evaporation lead to higher dye concentration at the surface of TiO<sub>2</sub> film<sup>105</sup>. The films obtained by electro spray took only a few minutes to process and showed similar absorbance to the conventional dye soaking method which takes 24 h. The electro spray method performed at a slightly higher efficiency than the conventional dye soaking process (3.9% vs. 3.5%).

Most of electro sprayed photolayer of DSSCs use the low concentration suspensions, ranging from 0.01% to

0.4%<sup>100, 106-107</sup>, meaning for each part of solid film to be deposited, 250 to 10000 parts of solvent must be evaporated, hindering the scale-up production because of extra costs of solvent recycling. In comparison, the continuous phase methods (i.e. doctor blading and spin coating) are able to process high concentration suspension in paste or slurry form. Zhu et al. report electro sprayed DSSC photo electrode from dense suspension of TiO<sub>2</sub> nanoparticles<sup>36</sup> of 40 wt% in EG, increasing the typical concentration of electro spray by ~1000x. The one-step electro sprayed active layer from dense suspensions is uniform in film thickness, while keeping the hierarchical nano/ micro-structures of multiple length scales, ranging from the clusters of (2±1) μm diameter micro spheres consists of 25 nm TiO<sub>2</sub> nanoparticles (Fig. 14). The key to the process is to control the drying to ensure complete solvent evaporation while avoiding formation of hollow particles.

Tang and Gomez conducted systematic study on the thin film morphology fabricated by electro spray drying colloidal TiO<sub>2</sub> nanoparticle suspensions<sup>37</sup>. They achieved remarkable controllability over the morphology by tuning three parameters: particle impact velocity, nanoparticle or cluster size, and solvent evaporation (Fig. 15). They found that the structure is governed by the relative importance of the external electric field induced particle drift and the thermal diffusion velocity due to Brownian motion. When the electric field derived velocity dominates, columnar structures are formed as a result of ballistic deposition, while when Brownian motion is more important, fractal-like structures are achieved. If the droplet evaporation time is tuned to allow for incomplete drying, the subsequent evaporation of the remaining solvent on the substrate produces films with high interconnectivity. Electro spray printed films have large-scale uniformity that is independent of thickness. In a separate work, Tang and Gomez studied the morphology's effect on the DSSCs' performance<sup>108</sup>. They found that generally, electro sprayed



**Fig. 13 | SEM image of the ZnO nanoparticles fabricated by (a) doctor-blade method and (b) large scale ZnO film prepared by electro spray technique after heat treated at 460 °C for 1 h<sup>104</sup>.**

DSSCs have higher  $V_{OC}$  and FF as compared to spin coated devices, whereas the latter exhibit higher  $I_{SC}$ . Electrochemical impedance spectroscopy suggested electro sprayed cells have larger recombination resistance and lower chemical capacitance. By synergistically combining the performance merits of the two methods, they made device with bilayer structure: with densely packed spin coated particles at the bottom where light absorption is critical, and a more porous electro sprayed layer on top, which facilitates hole transport in the electrolyte and light scattering for better optical absorption. In doing so, the bilayer device achieved higher efficiency than both electro sprayed and spin coated cells.

It is worth mentioning that although currently research

activities on DSSCs are not as active as OPV or perovskite solar cells, the study on the unique mesoporous electrode structure can still provide insights for many applications beyond photovoltaics, such as biomedical scaffolds<sup>109</sup>, gas sensors<sup>110</sup>, lithium ion batteries<sup>111</sup>, and photocatalysts for water splitting<sup>112</sup>. In those applications, the morphology of the multiscale films is critical for device performance, and the fundamentals learned from fabricating DSSCs photoelectrodes with controllable deposition of nanoparticles are still applicable. The interpretation of the morphologies in terms of relative importance of key physical process (electric field driven drift, Brownian motion, and evaporation) provides useful conceptual framework for rational design rules instead of try-and-error attempts.

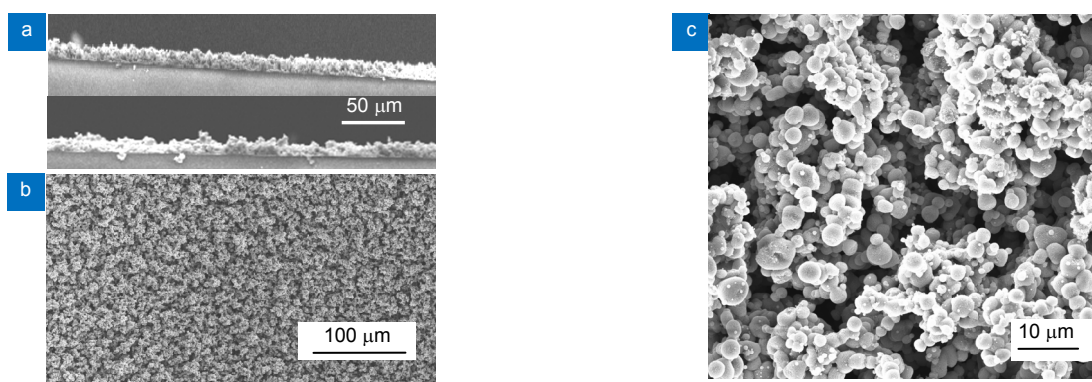


**Fig. 14 | Multiscale of porous structures fabricated by electro spraying dense P25 suspensions. SEM images of the electro sprayed film from dense P25 suspensions to the substrate heated at 150 °C and 250 °C<sup>36</sup>. (a) Side view of the film showing decent film uniformity. (b) Top view of the electro sprayed film. (c) Closeup of the electro sprayed film showing the multiscale nature of the photo electrode.**

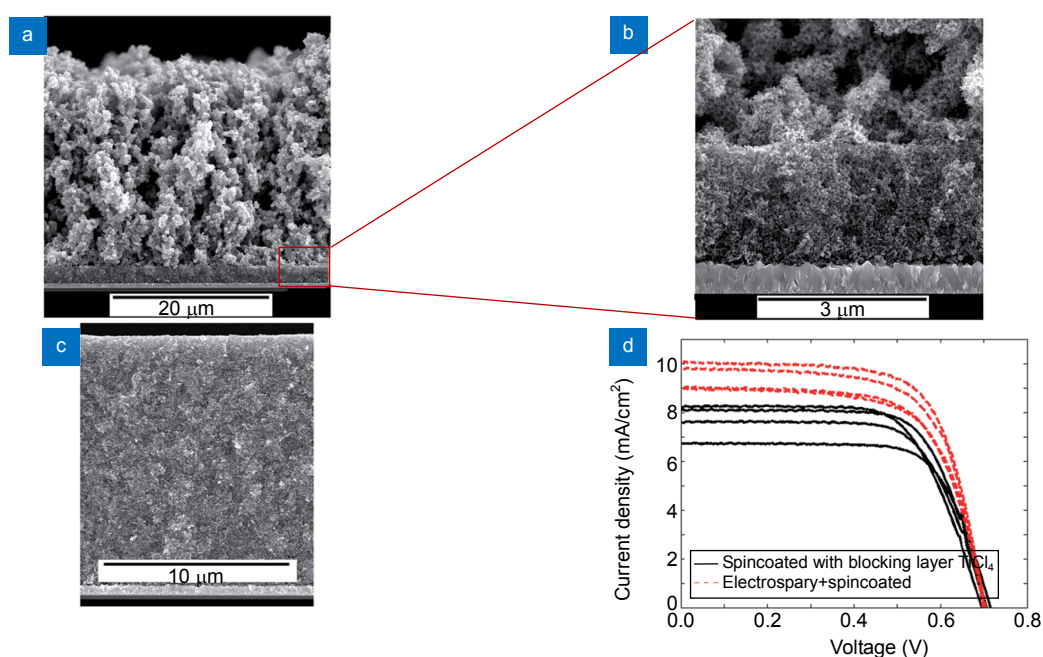


**Fig. 15 | Comparison of a hybrid electro spray and spin coated DSSC with bilayer structure with a purely spin coated one<sup>37</sup>. (a) SEM image of hybrid structure with close up of the interface in (b). (c) SEM cross section of a spin coated (5x) DSSC. (d)  $J-V$  characteristics comparing the two structures (with the spin coated cell having  $TiO_2$  blocking layers and  $TiCl_4$  treatment).**

## Summary and outlook

We have reviewed the progress of applying electrospray for fabricating three types of solution processible photovoltaics. The fact that electrospray can handle drastically different solutions of various types PV devices, ranging from low conductivity liquids of semiconducting polymer solutions to very highly conducting salt solution in polar solvents of perovskite precursor solutions, to the dense suspension of TiO<sub>2</sub> nanoparticles for DSSC. Such wide range of conductivity, viscosity, polarity of solvents, and solid contents demonstrate that electrospray is indeed a versatile fabrication method for PVs.

The comparison of the electrospray printing to doctor blading can provide some insights in choosing appropriate fabrication techniques for perovskite solar cells. Electrospayed polycrystalline perovskite film has grain size of only ~300 nm, which is comparable to one-step spin-coating but is smaller than that of leading results of doctor blading<sup>12</sup>. However, over 100x increase in grain boundary density did not drastically harm the PCE (15.0% for all-electrospray printed vs 20% for doctor blading), signifying the strong defect tolerance of perovskite<sup>113</sup>. Another important metric for fabrication methods is the printing speed. The optimal substrate moving speed is ~10 μm/s in the typical evaporation region of doctor blading. The speed can be increased to ~50 mm/s in the Landau-Levich region with surfactant additives that suppresses interfacial instability<sup>76</sup>. Electrospray printing is ~10 mm/s or higher, which is much faster than the doctor blading in the evaporating region which is most commonly seen in literature. The electrospray printing speed can be further increased by arrays of hundreds of electrospray emitters<sup>51</sup>.

There are a few challenges faced by the electrospray printing of photovoltaics. First and foremost, the mechanism of the ions formed in the Taylor cone and the electrochemistry effect is not well understood. Especially for the perovskite solutions, the current is relatively high, which suggests the amount of charge separated by the electrospray process is large per unit time. Although the printed perovskite solar cells do not show obvious composition or performance difference from spin coated ones, the electrochemistry effect of the solution under extended period time of electric charging is worthy of further investigation. Secondly, the choice of solvents is largely empirical and may have plenty room for optimization. To form a stable Taylor cone, the liquid solution must have

certain range of conductivity. However, available solvents are often limited by the solubility, which could be challenging for polymeric materials. Many solvents used in spin coating polymer solar cells are non-polar and does not provide sufficient electric conductivity. In such cases, conductivity booster could be added. Mixture of binary or ternary solvents could also be an effective way for providing the required solubility and conductivity.

Developing electrospray as a large scale process to fabricate OPVs, like the entire field of PV research, will require a truly interdisciplinary effort. Works reviewed here have demonstrated the unique advantages of using electrospray as a manufacturing tool in SPPVs, such as non-vacuum deposition, improved active layer morphology, and compatible with roll-to-roll process, while maintaining high PCE. The performances of the ES-SPPVs are dramatically affected by the morphology of the active layer. It is highly desirable to use smaller droplets, which may reduce the relic boundary density and thus the  $R_s$ . Multiplexed electrospays are indispensable in the scale up of electrospray deposition. Meanwhile, to further make electrospray a more competitive technique, significant research efforts should be made to better understand the fundamental physics such as the droplet heat and mass transfer, impact dynamics at the substrate, interaction of multiplexed electrospray sources, and reduction of space charge.

## References

1. Green M A, Ho-Baillie A, Snaith H J. The emergence of perovskite solar cells. *Nat Photonics* **8**, 506–514 (2014).
2. Huang J S, Shao Y C, Dong Q F. Organometal trihalide perovskite single crystals: a next wave of materials for 25% efficiency photovoltaics and applications beyond? *J Phys Chem Lett* **6**, 3218–3227 (2015).
3. Kojima A, Teshima K, Shirai Y, Miyasaka T. Organometal halide perovskites as visible-light sensitizers for photovoltaic cells. *J Am Chem Soc* **131**, 6050–6051 (2009).
4. Burschka J, Pellet N, Moon S J, Humphry-Baker R, Gao P et al. Sequential deposition as a route to high-performance perovskite-sensitized solar cells. *Nature* **499**, 316–319 (2013).
5. Green M A, Hishikawa Y, Dunlop E D, Levi D H, Hohl-Ebinger J et al. Solar cell efficiency tables (version 53). *Prog Photovoltaics* **27**, 3–12 (2019).
6. Cui Y, Yao H F, Zhang J Q, Zhang T, Wang Y M et al. Over 16% efficiency organic photovoltaic cells enabled by a chlorinated acceptor with increased open-circuit voltages. *Nat Commun* **10**, 2515 (2019).
7. Jiang K, Wei Q Y, Lai J Y L, Peng Z X, Kim H K et al. Alkyl chain tuning of small molecule acceptors for efficient organic solar cells. *Joule* **3**, 3020–3033 (2019).
8. Du X Y, Heumueller T, Gruber W, Classen A, Unruh T et al. Efficient polymer solar cells based on non-fullerene acceptors

- with potential device lifetime approaching 10 years. *Joule* **3**, 215–226 (2019).
- Gong J W, Liang J, Sumathy K. Review on dye-sensitized solar cells (DSSCs): Fundamental concepts and novel materials. *Renew Sust Energy Rev* **16**, 5848–5860 (2012).
  - Gu X D, Shaw L, Gu K, Toney M F, Bao Z N. The meniscus-guided deposition of semiconducting polymers. *Nat Commun* **9**, 534 (2018).
  - Zhang L, Lin B J, Hu B, Xu X B, Ma W. Blade-cast nonfullerene organic solar cells in air with excellent morphology, efficiency, and stability. *Adv Mater* **30**, 1800343 (2018).
  - Wu W Q, Wang Q, Fang Y J, Shao Y C, Tang S et al. Molecular doping enabled scalable blading of efficient hole-transport-layer-free perovskite solar cells. *Nat Commun* **9**, 1625 (2018).
  - Xu J, Wu H C, Zhu C X, Ehrlich A, Shaw L et al. Multi-scale ordering in highly stretchable polymer semiconducting films. *Nat Mater* **18**, 594–601 (2019).
  - Wu Q, Guo J, Sun R, Guo J, Jia S F et al. Slot-die printed non-fullerene organic solar cells with the highest efficiency of 12.9% for low-cost PV-driven water splitting. *Nano Energy* **61**, 559–566 (2019).
  - Zuo C T, Vak D, Angmo D, Ding L M, Gao M. One-step roll-to-roll air processed high efficiency perovskite solar cells. *Nano Energy* **46**, 185–192 (2018).
  - Yang J Y, Lin Y B, Zheng W H, Liu A L, Cai W Z et al. Roll-to-roll slot-die-printed polymer solar cells by self-assembly. *ACS Appl Mater Interfaces* **10**, 22485–22494 (2018).
  - Eggenhuisen T M, Galagan Y, Coenen E W C, Voorthuizen W P, Slaats M W L et al. Digital fabrication of organic solar cells by Inkjet printing using non-halogenated solvents. *Solar Energy Mater Solar Cells* **134**, 364–372 (2015).
  - Eggenhuisen T M, Galagan Y, Biezemans A F K V, Slaats T M W L, Voorthuizen W P et al. High efficiency, fully inkjet printed organic solar cells with freedom of design. *J Mater Chem A* **3**, 7255–7262 (2015).
  - Wei Z H, Chen H N, Yan K Y, Yang S H. Inkjet printing and instant chemical transformation of a  $\text{CH}_3\text{NH}_3\text{PbI}_3$ /nanocarbon electrode and interface for planar perovskite solar cells. *Angew Chem Int Ed* **53**, 13239–13243 (2014).
  - Liu A L, Zheng W H, Yin X L, Yang J Y, Lin Y B et al. Manipulate micrometer surface and nanometer bulk phase separation structures in the active layer of organic solar cells via synergy of ultrasonic and high-pressure gas spraying. *ACS Appl Mater Interfaces* **11**, 10777–10784 (2019).
  - Duan H X, Li C, Yang W W, Lojewski B, An L et al. Near-field electro-spray microprinting of polymer-derived ceramics. *J Microelectromech Syst* **22**, 1–3 (2013).
  - Zhao X Y, Tao Z, Yang W W, Xu K C, Wang L et al. Morphology and electrical characteristics of polymer: Fullerene films deposited by electro-spray. *Solar Energy Mater Solar Cells* **183**, 137–145 (2018).
  - Zhao X Y, Yang W W, Cheng L, Wang X Z, Lim S L et al. Effects of Damköhler number of evaporation on the morphology of active layer and the performance of organic heterojunction solar cells fabricated by electro-spray method. *Solar Energy Mater Solar Cells* **134**, 140–147 (2015).
  - Zheng J H, Zhang M, Lau C F J, Deng X F, Kim J et al. Spin-coating free fabrication for highly efficient perovskite solar cells. *Solar Energy Mater Solar Cells* **168**, 165–171 (2017).
  - Cloupeau M, Prunet-Foch B. Electrostatic spraying of liquids in cone-jet mode. *J Electrostat* **22**, 135–159 (1989).
  - Deng W W, Gomez A. The role of electric charge in microdroplets impacting on conducting surfaces. *Phys Fluids* **22**, 051703 (2010).
  - Fenn J B, Mann M, Meng C K, Wong S F, Whitehouse C M. Electro-spray ionization for mass spectrometry of large biomolecules. *Science* **246**, 64–71 (1989).
  - Taylor G I. Disintegration of water drops in an electric field. *Proc Roy Soc A Math Phys Eng Sci* **280**, 383–397 (1964).
  - Cloupeau M, Prunet-Foch B. Electrostatic spraying of liquids: Main functioning modes. *J Electrostat* **25**, 165–184 (1990).
  - De La Mora J F. The fluid dynamics of Taylor cones. *Annu Rev Fluid Mech* **39**, 217–243 (2007).
  - Gomez A, Deng W W. Fundamentals of cone-jet electro-spray. In *Aerosol Measurement: Principles, Techniques, and Applications 3rd ed* (Wiley, 2011); <https://doi.org/10.1002/9781118001684.ch20>.
  - De La Mora J F, Navascues J, Fernandez F, Rosell-Llompert J. Generation of submicron monodisperse aerosols in electro-sprays. *J Aerosol Sci* **21**, S673–S676 (1990).
  - Tang K Q, Gomez A. On the structure of an electrostatic spray of monodisperse droplets. *Phys Fluids* **6**, 2317–2332 (1994).
  - Sazhin S S. Advanced models of fuel droplet heating and evaporation. *Progress in Energy and Combustion Science*, **32**, 162–214 (2005).
  - Zhao X Y, Johnston D E, Rodriguez J C, Tao Z, Mi B X et al. Nanostructured semiconducting polymer films with enhanced crystallinity and reorientation of crystalline domains by electro-spray deposition. *Macromol Mater Eng* **302**, 1700090 (2017).
  - Zhu T J, Li C, Yang W W, Zhao X Y, Wang X L et al. Electro-spray dense suspensions of  $\text{TiO}_2$  nanoparticles for dye sensitized solar cells. *Aerosol Sci Technol* **47**, 1302–1309 (2013).
  - Tang J, Gomez A. Controlled mesoporous film formation from the deposition of electro-sprayed nanoparticles. *Aerosol Sci Technol* **51**, 755–765 (2017).
  - Gañán-Calvo A M, López-Herrera J M, Herrada M A, Ramos A, Montanero J M. Review on the physics of electro-spray: from electrokinetics to the operating conditions of single and coaxial Taylor cone-jets, and AC electro-spray. *J Aerosol Sci* **125**, 32–56 (2018).
  - Hartman R P A, Brunner D J, Camelot D M A, Marijnissen J C M, Scarlett B. Jet break-up in electrohydrodynamic atomization in the cone-jet mode. *J Aerosol Sci* **31**, 65–95 (2000).
  - Park S E, Kim S, Kim K, Joe H E, Jung B et al. Fabrication of ordered bulk heterojunction organic photovoltaic cells using nanopatterning and electrohydrodynamic spray deposition methods. *Nanoscale* **4**, 7773–7779 (2012).
  - Abramzon B, Sirignano W A. Droplet vaporization model for spray combustion calculations. *Int J Heat Mass Transfer* **32**, 1605–1618 (1989).
  - Yang W W, Lojewski B, Wei Y, Deng W W. Interactions and deposition patterns of multiplexed electro-sprays. *J Aerosol Sci* **46**, 20–33 (2012).
  - Deng W W, Klemic J F, Li X H, Reed M A, Gomez A. Increase of electro-spray throughput using multiplexed microfabricated sources for the scalable generation of monodisperse droplets. *J Aerosol Sci* **37**, 696–714 (2006).
  - Kim J S, Chung W S, Kim K, Dong Y K, Paeng K J et al. Solar cells: performance optimization of polymer solar cells using electrostatically sprayed photoactive layers (Adv. Funct. Mater. 20/2010). *Adv Funct Mater* **20**, 3402 (2010).

45. Lingam B, Babu K R, Tewari S P, Vaitheeswaran G, Lebègue S. Quasiparticle band structure and optical properties of NH<sub>3</sub>BH<sub>3</sub>. *Phys Status Solidi A* **5**, 10–12 (2011).
46. Zhao X Y, Wang X Z, Lim S L, Qi D C, Wang R et al. Enhancement of the performance of organic solar cells by electrospray deposition with optimal solvent system. *Solar Energy Mater Solar Cells* **121**, 119–125 (2014).
47. Jiang Y Y, Wu C C, Li L R, Wang K, Tao Z et al. All electrospray printed perovskite solar cells. *Nano Energy* **53**, 440–448 (2018).
48. Gao F, Yi H, Qi L H, Qiao R, Deng W W. Weakly charged droplets fundamentally change impact dynamics on flat surfaces. *Soft Matter* **15**, 5548–5553 (2019).
49. Kelly R T, Page J S, Zhao R, Qian W J, Mottaz H M et al. Capillary-based multi nanoelectrospray emitters: improvements in ion transmission efficiency and implementation with capillary reversed-phase LC-ESI-MS. *Anal Chem* **80**, 143–149 (2008).
50. Duby M H, Deng W W, Kim K, Gomez T, Gomez A. Stabilization of monodisperse electrosprays in the multi-jet mode via electric field enhancement. *J Aerosol Sci* **37**, 306–322 (2006).
51. Deng W W, Waits C M, Morgan B, Gomez A. Compact multiplexing of monodisperse electrosprays. *J Aerosol Sci* **40**, 907–918 (2009).
52. Hu H Q, Rangou S, Kim M, Gopalan P, Filiz V et al. Continuous equilibrated growth of ordered block copolymer thin films by electrospray deposition. *ACS Nano* **7**, 2960–2970 (2013).
53. Lozano P, Martínez-Sánchez M. On the dynamic response of externally wetted ionic liquid ion sources. *J Phys D: Appl Phys* **38**, 2371–2377 (2005).
54. Rebollo-Muñoz N, Montanero J M, Gañán-Calvo A M. On the use of hypodermic needles in electrospray. *EPJ Web Conf* **45**, 01128 (2013).
55. Sorensen G. Ion bombardment of electrosprayed coatings: an alternative to reactive sputtering? *Surf Coat Technol* **112**, 221–225 (1999).
56. Sen A, Darabi J, Knapp D, Liu J. Modeling and characterization of a carbon fiber emitter for electrospray ionization. *J Microeng Microev* **16**, 620–630 (2006).
57. Kallman H, Pope M. Photovoltaic effect in organic crystals. *J Chem Phys* **30**, 585–586 (1959).
58. Yu G, Gao J, Hummelen J C, Wudl F, Heeger A J. Polymer photovoltaic cells: enhanced efficiencies via a network of internal donor-acceptor heterojunctions. *Science* **270**, 1789–1791 (1995).
59. Heeger A J. Semiconducting polymers: the third generation. *Chem Soc Rev* **39**, 2354–2371 (2010).
60. Liang Y Y, Xu Z, Xia J B, Tsai S T, Wu Y et al. For the bright future-bulk heterojunction polymer solar cells with power conversion efficiency of 7.4%. *Adv Mater* **22**, E135–E138 (2010).
61. Siringhaus H, Brown P J, Friend R H, Nielsen M M, Bechgaard K et al. Two-dimensional charge transport in self-organized, high-mobility conjugated polymers. *Nature* **401**, 685–688 (1999).
62. Kim Y, Cook S, Tuladhar S M, Choulis S A, Nelson J et al. A strong regioregularity effect in self-organizing conjugated polymer films and high-efficiency polythiophene: fullerene solar cells. *Nat Mat* **5**, 197–203 (2006).
63. Hlaing H, Lu X H, Hofmann T, Yager K G, Black C T et al. Nanoimprint-induced molecular orientation in semiconducting polymer nanostructures. *ACS Nano* **5**, 7532–7538 (2011).
64. Johnston D E, Yager K G, Hlaing H, Lu X H, Ocko B M et al. Nanostructured surfaces frustrate polymer semiconductor molecular orientation. *ACS Nano* **8**, 243–249 (2014).
65. Fukuda T, Suzuki K, Yoshimoto N, Liao Y J. Controlled donor-acceptor ratio for application of organic photovoltaic cells by alternative intermittent electrospray co-deposition. *Org Electron* **33**, 32–39 (2016).
66. Fukuda T, Toda A, Takahira K, Suzuki K, Liao Y J et al. Molecular ordering of spin-coated and electrosprayed P3HT: PCBM thin films and their applications to photovoltaic cell. *Thin Solid Films* **612**, 373–380 (2016).
67. Fukuda T, Toda A, Takahira K, Kuzuhara D, Yoshimoto N. Improved performance of organic photovoltaic cells with PTB7-Th: PC<sub>71</sub>BM by optimized solvent evaporation time in electrospray deposition. *Org Electron* **48**, 96–105 (2017).
68. Takahira K, Toda A, Suzuki K, Fukuda T. Highly efficient organic photovoltaic cells fabricated by electrospray deposition using a non-halogenated solution. *Phys Status Solidi A* **214**, 1600536 (2017).
69. Khanum K K, Anakkavoor Krishnaswamy J, Ramamurthy P C. Design and fabrication of photonic structured organic solar cells by electrospraying. *J Phys Chem C* **121**, 8531–8540 (2017).
70. Kimoto A, Takaku H, Hayakawa H, Koseki M, Ishihama R et al. Multilayer organic photovoltaic devices fabricated by electrospray deposition technique and the role of the interlayer. *Thin Solid Films* **636**, 302–306 (2017).
71. Hong S C, Lee G, Ha K, Yoon J, Ahn N et al. Precise morphology control and continuous fabrication of perovskite solar cells using droplet-controllable electrospray coating system. *ACS Appl Mater Interfaces* **9**, 7879–7884 (2017).
72. Lin P Y, Chen Y Y, Guo T F, Fu Y S, Lai L C et al. Electrospray technique in fabricating perovskite-based hybrid solar cells under ambient conditions. *RSC Adv* **7**, 10985–10991 (2017).
73. Kavadiya S, Niedzwiedzki D M, Huang S, Biswas P. Electrospray-assisted fabrication of moisture-resistant and highly stable perovskite solar cells at ambient conditions. *Adv Energy Mater* **7**, 1700210 (2017).
74. Hsu K C, Lee C H, Guo T F, Chen T H, Fang T H et al. Improvement efficiency of perovskite solar cells by hybrid electrospray and vapor-assisted solution technology. *Org Electron* **57**, 221–225 (2018).
75. Han S, Kim H, Lee S, Kim C. Efficient planar-heterojunction perovskite solar cells fabricated by high-throughput sheath-gas-assisted electrospray. *ACS Appl Mater Interfaces* **10**, 7281–7288 (2018).
76. Deng Y H, Zheng X P, Bai Y, Wang Q, Zhao J J et al. Surfactant-controlled ink drying enables high-speed deposition of perovskite films for efficient photovoltaic modules. *Nat Energy* **3**, 560–566 (2018).
77. He M, Li B, Cui X, Jiang B B, He Y J et al. Meniscus-assisted solution printing of large-grained perovskite films for high-efficiency solar cells. *Nat Commun* **8**, 16045 (2017).
78. Li J B, Munir R, Fan Y Y, Niu T Q, Liu Y C et al. Phase transition control for high-performance blade-coated perovskite solar cells. *Joule* **2**, 1313–1330 (2018).
79. Hwang K, Jung Y S, Heo Y J, Scholes F H, Watkins S E et al. Toward large scale roll-to-roll production of fully printed perovskite solar cells. *Adv Mater* **27**, 1241–1247 (2015).
80. Yang Z B, Chueh C C, Zuo F, Kim J H, Liang P W et al. High-performance fully printable perovskite solar cells via blade-coating technique under the ambient condition. *Adv Energy Mater* **5**, 1500328 (2015).
81. Qin T S, Huang W C, Kim J E, Vak D, Forsyth C et al. Amorphous hole-transporting layer in slot-die coated perovskite solar

- cells. *Nano Energy* **31**, 210–217 (2017).
82. Mei A Y, Li X, Liu L F, Ku Z L, Liu T F et al. A hole-conductor-free, fully printable mesoscopic perovskite solar cell with high stability. *Science* **345**, 295–298 (2014).
83. Lee J W, Na S I, Kim S S. Efficient spin-coating-free planar heterojunction perovskite solar cells fabricated with successive brush-painting. *J Power Sources* **339**, 33–40 (2017).
84. Jung Y S, Hwang K, Heo Y J, Kim J E, Lee D et al. One-step printable perovskite films fabricated under ambient conditions for efficient and reproducible solar cells. *ACS Appl Mater Interfaces* **9**, 27832–27838 (2017).
85. Bashir A, Shukla S, Lew J H, Shukla S, Bruno A et al. Spinel Co<sub>3</sub>O<sub>4</sub> nanomaterials for efficient and stable large area carbon-based printed perovskite solar cells. *Nanoscale* **10**, 2341–2350 (2018).
86. O'Regan B, Grätzel M. A low-cost, high-efficiency solar cell based on dye-sensitized colloidal TiO<sub>2</sub> films. *Nature* **353**, 737–740 (1991).
87. Bach U, Lupo D, Comte P, Moser J E, Weissörtel F et al. Solid-state dye-sensitized mesoporous TiO<sub>2</sub> solar cells with high photon-to-electron conversion efficiencies. *Nature* **395**, 583–585 (1998).
88. Hagfeldt A, Grätzel M. Molecular photovoltaics. *Acc Chem Res* **33**, 269–277 (2000).
89. Grätzel M. Photoelectrochemical cells. *Nature* **414**, 338–344 (2001).
90. Grätzel M. Conversion of sunlight to electric power by nanocrystalline dye-sensitized solar cells. *J Photochem Photobiol A: Chem* **164**, 3–14 (2004).
91. Sonai G G, Tiihonen A, Miettunen K, Lund P D, Nogueira A F. Long-term stability of dye-sensitized solar cells assembled with cobalt polymer gel electrolyte. *J Phys Chem C* **121**, 17577–17585 (2017).
92. Kakiage K, Aoyama Y, Yano T, Oya K, Fujisawa J I et al. Highly-efficient dye-sensitized solar cells with collaborative sensitization by silyl-anchor and carboxy-anchor dyes. *Chem Commun* **51**, 15894–15897 (2015).
93. Widodo S, Wiranto G, Hidayat M N. Fabrication of dye sensitized solar cells with spray coated Carbon Nano Tube (CNT) based counter electrodes. *Energy Procedia* **68**, 37–44 (2015).
94. Kabir F, Sakib S N, Matin N. Stability study of natural green dye based DSSC. *Optik* **181**, 458–464 (2019).
95. Ito S, Murakami T N, Comte P, Liska P, Grätzel C et al. Fabrication of thin film dye sensitized solar cells with solar to electric power conversion efficiency over 10%. *Thin Solid Films* **516**, 4613–4619 (2008).
96. Kim Y J, Lee M H, Kim H J, Lim G, Choi Y S et al. Formation of highly efficient dye - sensitized solar cells by hierarchical pore generation with nanoporous TiO<sub>2</sub> spheres. *Adv Mater* **21**, 3668–3673 (2009).
97. Fujimoto M, Kado T, Takashima W, Kaneto K, Hayase S. Dye-sensitized solar cells fabricated by electro-spray coating using TiO<sub>2</sub> nanocrystal dispersion solution. *J Electrochem Soc* **153**, A826–A829 (2006).
98. Zhang Y Z, Wu L H, Xie E Q, Duan H G, Han W H et al. A simple method to prepare uniform-size nanoparticle TiO<sub>2</sub> electrodes for dye-sensitized solar cells. *J Power Sources* **189**, 1256–1263 (2009).
99. Sudhagar P, Asokan K, Jung J H, Lee Y G, Park S et al. Efficient performance of electrostatic spray-deposited TiO<sub>2</sub> blocking layers in dye-sensitized solar cells after swift heavy ion beam irradiation. *Nanoscale Res Lett* **6**, 30 (2011).
100. Hwang D, Lee H, Jang S Y, Jo S M, Kim D et al. Electro-spray preparation of hierarchically-structured mesoporous TiO<sub>2</sub> spheres for use in highly efficient dye-sensitized solar cells. *ACS Appl Mater Interfaces* **3**, 2719–2725 (2011).
101. Huang F Z, Chen D H, Zhang L X, Caruso R A, Cheng Y B. Dual-function scattering layer of submicrometer-sized mesoporous TiO<sub>2</sub> beads for high-efficiency dye-sensitized solar cells. *Adv Funct Mater* **20**, 1301–1305 (2010).
102. Chen D H, Huang F Z, Cheng Y B, Caruso R A. Mesoporous anatase TiO<sub>2</sub> beads with high surface areas and controllable pore sizes: a superior candidate for high-performance dye-sensitized solar cells. *Adv Mater* **21**, 2206–2210 (2009).
103. Chou T P, Zhang Q, Fryxell G E, Cao G Z. Hierarchically structured ZnO film for dye-sensitized solar cells with enhanced energy conversion efficiency. *Adv Mater* **19**, 2588–2592 (2007).
104. Sheng X, Zhao Y, Zhai J, Jiang L, Zhu D. Electro-hydrodynamic fabrication of ZnO-based dye sensitized solar cells. *Appl Phys A* **87**, 715–719 (2007).
105. Hong J T, Seo H, Lee D G, Jang J J, An T P et al. A nano-porous TiO<sub>2</sub> thin film coating method for dye sensitized solar cells (DSSCs) using electrostatic spraying with dye solution. *J Electrostat* **68**, 205–211 (2010).
106. Hogan C J, Biswas P. Porous film deposition by electrohydrodynamic atomization of nanoparticle sols. *Aerosol Sci Technol* **42**, 75–85 (2008).
107. Modesto-Lopez L B, Biswas P. Role of the effective electrical conductivity of nanosuspensions in the generation of TiO<sub>2</sub> agglomerates with electro-spray. *J Aerosol Sci* **41**, 790–804 (2010).
108. Tang J, Gomez A. Control of the mesoporous structure of dye-sensitized solar cells with electro-spray deposition. *J Mater Chem A* **3**, 7830–7839 (2015).
109. Chan B P, Leong K W. Scaffolding in tissue engineering: general approaches and tissue-specific considerations. *Eur Spine J* **17**, 467–479 (2008).
110. Bochenkov V E, Sergeev G B. Sensitivity, selectivity, and stability of gas-sensitive metal-oxide nanostructures. In *Metal Oxide Nanostructures and Their Applications* (American Scientific Publishers, 2010).
111. Tang J, Liu W, Wang H L, Gomez A. High performance metal oxide–graphene hybrid nanomaterials synthesized via opposite-polarity electro-sprays. *Adv Mater* **28**, 10298–10303 (2016).
112. Li X M, Hao X G, Abudula A, Guan G Q. Nanostructured catalysts for electrochemical water splitting: current state and prospects. *J Mater Chem A* **4**, 11973–12000 (2016).
113. Kovalenko M V, Protesescu L, Bodnarchuk M I. Properties and potential optoelectronic applications of lead halide perovskite nanocrystals. *Science* **358**, 745–750 (2017).

### Acknowledgements:

X.Z. acknowledges the funding support from National Science Foundation of China (NSFC) (No. 61975073 and No. 61605076). W. D. thanks the financial support from NSFC (No. 11872199 and No. 11932009).

### Competing interests

The authors declare no competing financial interests.